Title
Field Emission from Superfocused Surface Plasmon Polaritons on Scanning Probe Tips

Author
Majors, Julia Hannah

Publication Date
2014

UNIVERSITY OF CALIFORNIA,
IRVINE

Field Emission from Superfocused Surface Plasmon Polaritons on Scanning Probe Tips

THESIS

submitted in partial satisfaction of the requirements
for the degree of

MASTER OF SCIENCE

in Chemical and Material Physics - Physics

by

Julia H. Majors

Thesis Committee:
Professor V. Ara Apkarian, Chair
Professor Eric O. Potma
Professor Craig Martins

2014

DEDICATION

To my parents. Words cannot express my gratitude for the life they provided.

TABLE OF CONTENTS

LIST OF FIGURES

Page

LIST OF TABLES

ACKNOWLEDGMENTS

I am thankful to my advisor, Professor Ara Apkarian for providing me with so many opportunities and guiding me through this experiment. Without his help and push this work would not exist. I would like to thank Dr. Joonhee Lee, Professor's Eric Potma, Craig Martins, and Wytze van der for being immense source of knowledge and guidance. Thanks go to Stephen Sasaki for building the vacuum chamber and Professor Law and Dr. Zheng for their help with FIB etching at the LEXI facility. Thank you to Kevin, my current office mate, for stepping up and filling the big shoes left behind by Dr. Ale Rodriguez Perez, my closest scientist comrade and partner through this experiment. His kindness, wisdom, patience, and knowledge know no bounds and I am forever grateful to have worked with him and gained his friendship. Thanks to fellow members of the Apkarian lab as well as friends and family, without whose support this work could never be done. I would finally like to acknowledge the funding that made my research possible, provided by the National Science Foundation for the center for Chemistry at the Space-Time Limit (CHE-082913)

CURRICULUM VITAE

Julia H. Majors

ABSTRACT OF THE THESIS

Field Emission from Superfocused Surface Plasmon Polaritons on Scanning Probe Tips

By

Julia H. Majors

Master of Science in Chemical and Material Physics - Physics

University of California, Irvine, 2014

Professor V. Ara Apkarian, Chair

Field emission takes place upon focusing propagating surface plasmon polaritons (SPP) at the apex of a sharp metal tip. The effect is demonstrated with remotely launched SPPs on silver and gold probe tips. We couple femtosecond laser pulses through a grating inscribed on the taper of a smooth, silver wire 30um from the apex. Field-emitted current is directly correlated with the radiation of the super-focused SPP at the apex. Both current and radiation at the apex are measured as a function of incident polarization on the grating. In the absence of incident light at the apex, the local field of the ?naked? surface plasmon modulates the tunneling barrier that drives the field emission. We give a detailed analysis of the governing dynamics in the presence and absence of an applied extractor field, and aim to distinguish between mechanisms governing measured current. Independent of the distribution of the electrons in the metal half-space the emission acquires coherence by the time-dependent field of the plasmon in the vacuum half-space.

Chapter 1

Background and Motivation

1.1 Motivation

Scanning Tunneling Microscopes (STMs) provide beautiful images of single molecules with angstrom resolution showing full topology and structure [4, 5, 7]. Measuring dynamics with this resolution requires control of electron emission processes within the sub nm tunneling junction. With the continuing advancement in ultrafast optics, much focus has been placed on plasmonics and field emission properties of metallic probe tips [11, 24, 30, 31]. Coherent attosecond electron emission from a probe tip has been demonstrated [2, 17], but there are yet many challenges to overcome to make such tips appropriate for single molecule detection and imaging. The fundamental dynamics governing plasmons themselves, in the quantum regime, are not yet fully understood, especially in the regime of fields where photo-emissive processes transition into the tunneling regime.

Here, we demonstrate the use of nonlocal, propagating plasmon modes on cone structures. In this geometry, plasmons become super focused and spatially confined on the necessary angstrom scale, to produce electrons free from background radiation. These nano emitters, coupled with STM technology, would provide a direct window through which we can view the quantum world as it exists, mapping it more directly than ever to the human intellect.

I will first describe the governing principles fundamental to structure and dynamics of these nano emitters. This centers around the resonant interaction of light with metals, namely silver and gold, and I will begin with a discussion of the their electronic responses to electric fields and the processes by which fields cause electrons to escape the work function and emit. I will then describe the experimental design and procedures for measuring electrons emitted by plasmonic fields, followed by experimental results and the demonstration of remotely launched SPP controlled electron emission. This mechanism has potential applications in the direct fs control of tunneling electrons of a STM image.

1.2 Plasmonics

The dissociative behavior of electrons in periodic structures, like metals, produces a fluid-like system of delocalized charge density known as the Fermi sea. Within this fluid exists the possibility of electron density waves, forming areas of concentrated negative charge next to the concentrated positive charges that must follow behind. Under the right conditions, these waves can propagate along the physical surface of the metal and it becomes a system manipulatable by waveguiding techniques, notably, focusing. These quantized propagating modes, known as Surface Plasmon Polaritons (SPPs), are excitable on gold and silver using visible light. It is this property we wish to exploit in converting light into plasmonic fields, confining, and therefore enhancing it to its spatial limits at the apex of metallic tip. It is here we wish to produce a field high enough to allow coherent electrons to tunnel into vacuum and be collected as current.

1.2.1 Plasmons - Electron density oscillations

Surface Plasmon Polaritons

Optical properties of plasmonically active noble metals have been the focus of many thorough discussions in literature, having much interest in their ability to produce highly confined oscillating fields[19]. The Drude model of the electrons in nobel metals, after accounting for interband transitions, gives an accurate description for the dielectric response, $\epsilon(\omega)$, of these metals. This response is directly related to the natural frequency of the bulk free electron gas, also known as the plasma frequency, ω_p [21].

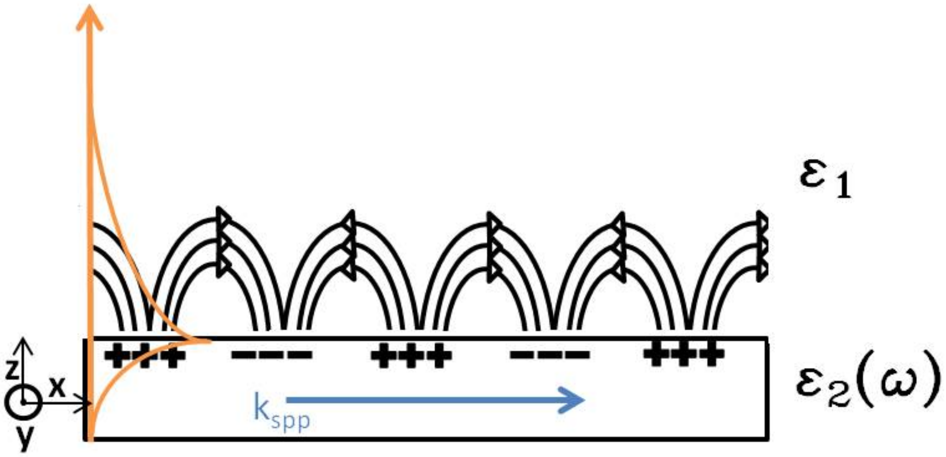

Figure 1.1: Diagram of a TM mode of the electromagnetic field at metal-vacuum interface. The field must decay exponentially into the half spaces above and below the interface in the $\vec{z}$ direction.

This response also tells us about the response of the electrons at the surface of these metals, those we wish to utilize here. Let's first look at the general case of an electromagnetic wave propagating along the surface of a planar metal, at the interface of a surrounding dielectric, as show in Fig.1.1. We use vacuum as the dielectric here and for the remainder of this text, both for simplicity and to relate to the experiment. Solutions to Maxwell's equations for a

TM mode, describing wavelike behavior along the interface and decaying exponentially in the perpendicular directions as described in Eq. (1.1), require the continuity of the parallel components of the electric field, $\vec{E}$, and the perpendicular components of the displacement vector across the interface. Solutions only exist for this mode, as discussed in [32].

$$\vec{E}_i = (E_x^j, 0, E_z^j)\ \exp[\,ik_x\, x \mp k_z^j\, z - i\omega t], \qquad j = 1, 2. \tag{1.1a}$$

$$\vec{H}_i = (0, H_y^j, 0)\ \exp[\,ik_x\, x \mp k_z^j\, z - i\omega t], \qquad j = 1, 2. \tag{1.1b}$$

Here, j is an index to indicate the two materials (metal or vacuum) in which the field is being described, where k_z^j determines the decay length of the electric field away from the interface. Continuity of the displacement yields:

$$\frac{k_{z1}}{k_{z2}} = -\frac{\epsilon_1(\omega)}{\epsilon_2} \tag{1.2}$$

Eq. (1.2) determines the real part of the two dielectric values must be opposite in sign. As is the case for most dielectrics, the dielectric constant for vacuum is positive, requiring the (real part of the) frequency dependent dielectric function of the metal to be negative. For each j, momentum conservation is represented by:

$$k_x^2 + k_{zj}^2 = \epsilon_i \frac{\omega^2}{c^2}, \qquad i = 1, 2. \tag{1.3}$$

By putting Eq.(1.2) into Eq.(1.3) we arrive at an expression for the dispersion of the SPP,

$$k_x^2 = \frac{\omega^2}{c^2} \frac{\epsilon_1(\omega)\epsilon_2}{\epsilon_1(\omega) + \epsilon_2}, \tag{1.4}$$

for $k_{spp} = k_x$. $\epsilon(\omega)$, having both real and imaginary components, leads to a complex k_{spp}

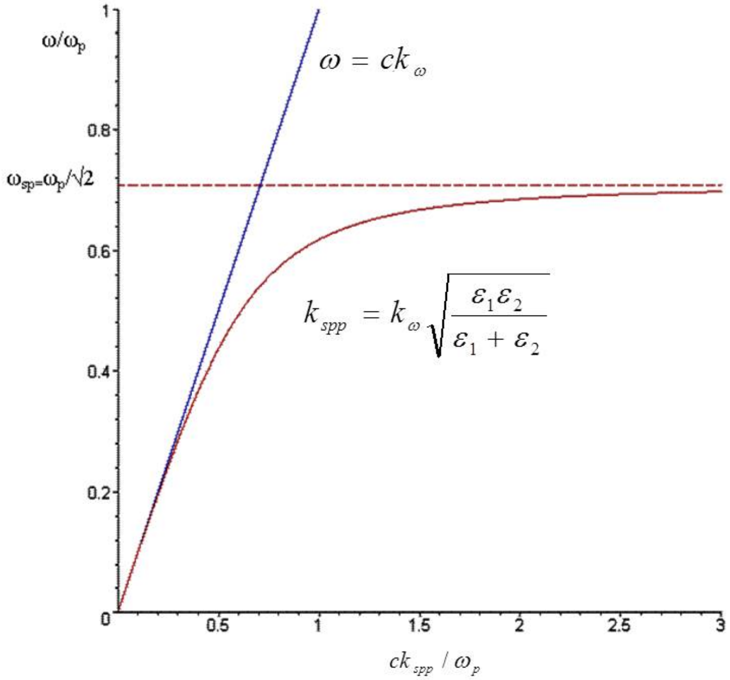

Figure 1.2: Dispersion curve for a generalized picture of SPP on metal-dielectric interface. k_{light} is shown in blue. The dispersion curve coincides with the upper branch of the SPP when $\omega = \omega_p$. Dashed line represent the surface plasmon frequency.

value whose components are given by the following equations:

$$k'_{spp} = \frac{\omega}{c}\sqrt{\frac{\epsilon'_1\epsilon_2}{\epsilon'_1+\epsilon_2}} \tag{1.5a}$$

$$k''_{spp} = \frac{\omega}{c}\left(\frac{\epsilon'_1\epsilon_2}{\epsilon'_1+\epsilon_2}\right)^{3/2}\frac{\epsilon''_1}{2{\epsilon'_1}^2}. \tag{1.5b}$$

Note, $\frac{{\epsilon''_1}^2}{{\epsilon'_1}^2} \simeq 0$. (1.5a) describes the real dispersion and wave vector that must be matched in order to excite this SPP. Fig.1.2 shows a plot of $k_{spp}(\omega)$ for silver and gold as well as the k_{light} line in vacuum, using dielectric values from reference [13]. For large values of k, where the group velocity, $\frac{d\omega}{dk} \to 0$, these curves asymptotically approach the value of the surface plasmon, ω_{sp}, for an electrostatic wave from the solution in the non-retarded regime where $c \to \infty$. This is referred to as the frequency of the surface plasmon (SP).

The complex part of k_{spp}, (1.5b), describes the damping of the wave and therefore determines the propagation length of the SPP. If we define the $1/e$ decay of the wave as the propagation length, $\lambda_{spp} = \frac{1}{k_{spp}}$. For many ultrafast optical experiments, including the one I discuss here, Ti:saph lasers are used to produce short pulses with a central wavelength $\simeq$ 800 nm. For this color, gold and silver with dielectric values ϵ_{Au} (800nm)$= -24 + 1.4i$ and ϵ_{Ag} (800 nm)$= -31 + .4i$. The decay length,λ_{spp} for gold in vacuum is $\sim 50\,\mu\text{m}$ whereas for silver is $\sim 300\,\mu\text{m}$. This number only decreases for other dielectric materials, as the value of ϵ_2 increases.

To understand the confinement at the surface, we'll look at decay length of the SPP k_z, perpendicular to the interface. (1.2) and (1.3) give:

$$k_z^i = \frac{\omega}{c}\sqrt{\frac{\epsilon_i'^2}{\epsilon_1' + \epsilon_2}}. \tag{1.6}$$

Eq. (1.6) tells us that for visible wavelengths the SPP in gold and silver field will decay much faster in the metal than the vacuum. At the 800 nm used in this experiment, for example, $\lambda_z^1 \sim 22$ nm, $\lambda_z^2 \sim 700$ nm. Typical enhancement factors at the surface are $\simeq 10^2 E_0$ [21].

Localized Surface Plasmons

Discussions of plasmonics are necessarily focused towards the nanoscale, so let's look now at the case of surface confined oscillations on particles and structures whose physical dimensions lie in this regime. In the simplest case of a nanometer sized sphere, where the wavelength of the oscillation is much larger than the sphere's radius, Maxwell's equations simplify in the non-retarded regime to Laplace's equation; the static solutions. Resonant modes in this regime, localized to the particle, are referred to as localized surface plasmons. The dispersion relation in this case gives a single valued dispersion relation:

$$\frac{\epsilon(\omega)}{\epsilon_2} = -\frac{l+1}{l} \tag{1.7}$$

From this, we can calculate the resonant frequency of our dipole.

$$\omega_{lsp} = \omega_p \left[\frac{l}{\epsilon_0(l+1)+l} \right]^{\frac{1}{2}}, \qquad l = 1, 2, ... \tag{1.8}$$

These localized modes are given by (1.8), where the value for l indicates the mode and is well approximated by only the $l = 1$, the dipole, mode for these particles of this size. For larger particles, higher order terms will play a role, but it is interesting to note the limit of ω_{lsp} is the ω_{sp} found as $k \to \infty$ for the SPP picture. In the small particle regime, plasmonic resonances are highly sensitive to the size and local structure. If we deviate from this ideal spherical picture, we can no longer think of the system as a point dipole with polarizability P. An aspect ratio $\neq 1$ for the spatial axes shifts the resonance and introduces a polarization dependence of the driving field from the differences in polarizability between the particle's three axes[19, 34]. In this case, the dipole frequencies along each axis can be calculated using $\frac{\epsilon(\omega)}{\epsilon_2} = 1 - \frac{1}{L_j}$, where L_j is a "depolarization" factor to account for shape and j indicates the axis. For larger particles, $>\sim 100nm$, the non-retarded solutions are no longer sufficient.

1.2.2 Excitation with light

Both the SPP and LP oscillations require excitation by an external injection of energy. In the case of the LP, with electrostatic solutions, excitation of the LP modes require only a matching of energy. In the case of the SPP, on the other hand, both energy and momentum must be considered for excitation. Incident light on a flat metal surface cannot excite propagating modes because the SPP k-vector, described previously by Eq.(1.5a), will always be larger than that of the incident light for a given frequency. In other words, the SPP dispersion line lies to the right of the light line for all frequencies. There are two principle methods of overcoming this mismatch and providing the dispersion overlap, one uses tunneling photons and the other uses diffraction from a periodic structure. The first requires placing the metal as a film on a prism to excite a propagating mode at the metal-vacuum interface from tunneled photons as shown in Fig. 1.3a. The in-plane component of the light vector at this interface excites the SPP with k-vector now given by,

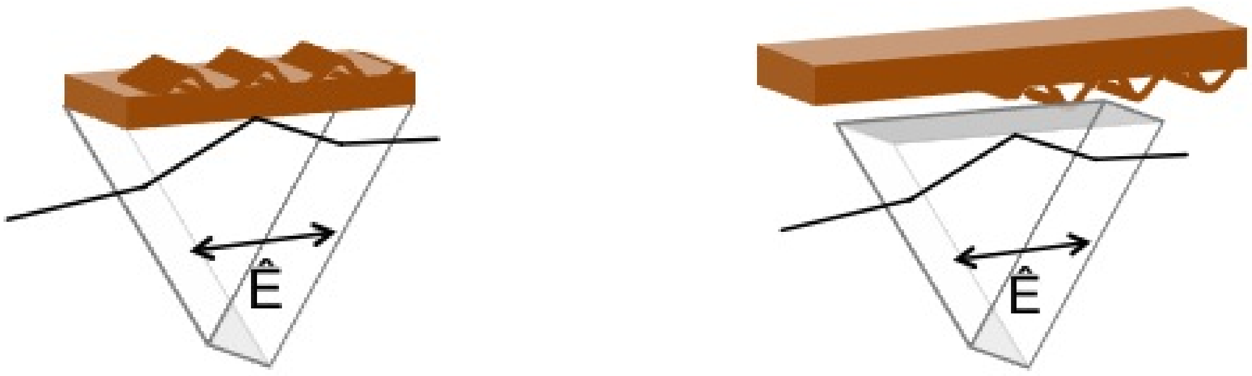

(a) Kretschmann geometry

(b) Otto geometry

Figure 1.3: Light enters a prism at the total internal reflection angle and tunnels through either the film thickness in the Kretschmann geometry (a), or the vacuum gap in the Otto configuration (b), exciting an SPP mode at the metal-vacuum interface with wave vector, $k_{spp} = \frac{\omega}{c}\sqrt{\epsilon_{pr}}\sin(\theta)$

$$k_{app} = k_{light}\sin\theta\sqrt{\epsilon_{pr}} = \frac{\omega}{c}\sqrt{\epsilon_{pr}}\sin\theta \tag{1.9}$$

where ϵ_{pr} is the dielectric constant of the prism and θ is the angle of incidence. The same result can also be achieved by separating the metal from the prism by a distance small enough that light can tunnel through the gap, as opposed to the metal, to excite the SPP mode at the incident metal-vacuum interface. This is known as an Otto configuration and is show in Fig.1.3b [32].

Unfortunately, prism techniques cannot be employed practically in tip geometries, but coupling methods using diffraction of incident light can be implemented with relative ease. Diffracted light from a periodic structure on the metal surface will gain a momentum contribution to the in-plane component of the light, determined by the grating wave vector and incidence angle. The generic grating equation is given as:

$$m\lambda = \Lambda(\sin\theta_i + \sin\theta_m) \qquad m = 1, 2, ... \tag{1.10}$$

for a grating spacing Λ, wavelength λ, incident and reflected angles $\theta_{i,m}$, and diffraction order, m. We can re-write Eq.(1.10) in terms of our k-vectors, using the relation $k_{gr} = \frac{2\pi}{a}$, as:

$$k_{diff} = \zeta_{pol}(k_{light}\sin\theta_i) + mk_{gr} \qquad m = 1, 2, ... \tag{1.11}$$

where I've added a polarization dependent term, $0 \leq \zeta_{pol} \leq 1$, that is maximized for P-polarization. SPP coupling will occur for values $k_{spp} = k_{grating}$. In the case of prism matching the slope of the light line was effectively shifted by the medium from which photons would be tunneling in order to intercept with the SPP dispersion curve. With grating matching, it is perhaps easier to think of the matching condition as met by intersecting the original light line with a new branch of the now periodic dispersion curve that can be described in a Brillouin picture (reciprocal space), as shown in Fig.1.4. For a given incidence angle, Λ can be tuned for the desired frequency, ω_{spp}.

Experimentally, gratings on metal films or surfaces are often made by ion beam etching [23]. For a broadband source of incident light, a fan shaped grating can expand the range of incidence angles and frequencies to which it can couple light to SPPs. As shown in Fig. 1.5, for a spot size large enough to illuminate at least a few grating grooves, a spacing that expands from 740-1000 nm can couple light from 750-850 nm over a 20° span.

Just as radiation can excite plasmonic modes, so can plasmonic modes decay to emit radiation. This is simplest for the case of a dipole-like LSP. Mie scattering provides good estimates

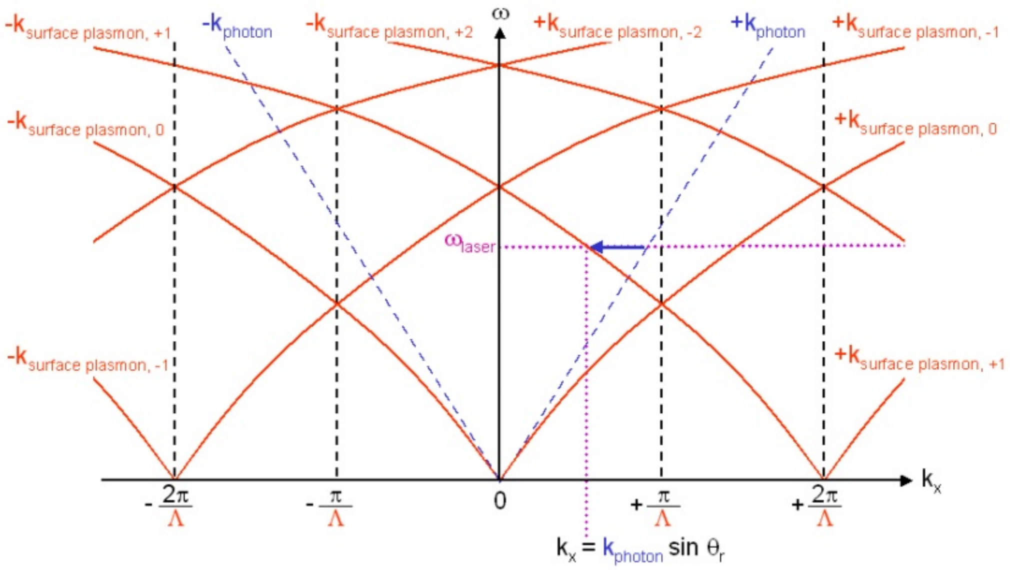

Figure 1.4: Dispersion relation in reciprocal space for SPP coupling via diffraction from a grating. The periodicity is determined by the grating spacing, Λ, which determines where incident light with in-plane component $k_{light} \sin theta_i$ (purple line) will intersect with one of the dispersion branches. Λ must be chosen such that this intersection occurs for for desired SPP frequency and incidence angle.

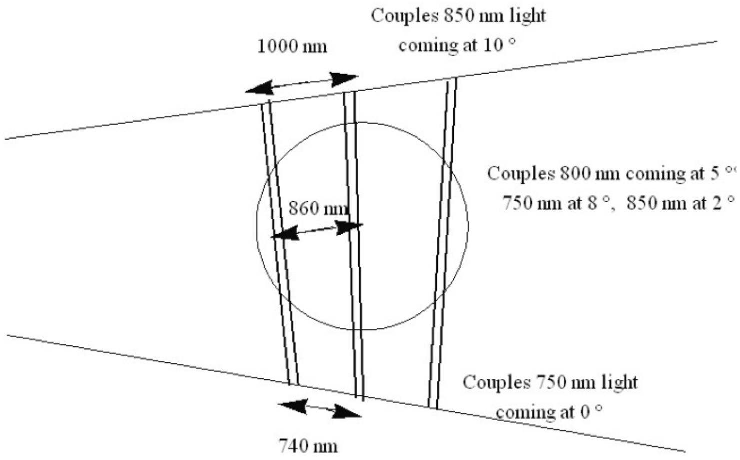

Figure 1.5: Depiction of laser spot on fan-shaped grating for SPP coupling to couple a larger range of incident frequencies and angles.

of radiation damping rates for most metals, with some corrections needed for particle sizes < 80 nm, especially in silver[27].

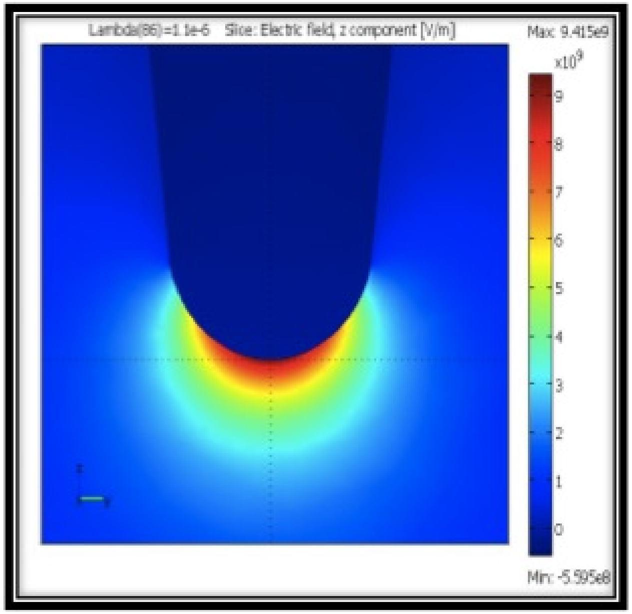

Figure 1.6: Field enhancement,$\frac{E}{E_0}$,on a nanometer sized tip in the direction of the tip axis.

1.2.3 Superfocusing Tip Geometry

The geometry of a cone provides a unique method of further enhancing the local field of a 2-D SPP wave in 3-D. The conical shape can act as a lens, focusing the SPP by adiabatically slowing the wave and confining the excitation volume. Theoretical enhancements of this focusing waveguide are reported at the apex of $10^3 E_0$, the incident field, in the direction of propagation (along the tip axis) [28]. This approach to producing high fields at the apex takes advantage of the volume confinement at the tip as well as the tunable, high efficiency coupling provided by 2-D coupling.

Experimentally, fields sufficient for the nonlinear frequency doubling of emitted light have been reported [24]. Although the infinitely sharp tip used in theoretical calculations, with a singularity at the apex, can't be used to describe the local field at the emitting radius in experiment, we can still use a dipole-like LSP picture to model a more realistic picture of local fields.

1.3 Electron Emission

Electrons are photo-emitted from a metal if they are able to absorb sufficient photon energy to overcome the work function. In the presence of sufficiently high fields, the work function of a metal is suppressed to allow the tunneling of electrons through the potential barrier, escape over it by the absorption of now fewer photons, or a combination of the two.

1.3.1 Mechanisms

In the case of incident radiation on a metallic tip like that of Fig.1.6, the mechanisms by which electrons may emit are depicted in Fig.1.7. In general, there are two regimes in which we can describe the electronic response of a metal to an optical field, each with its own set of available electron emission mechanisms. The two regimes are described by the Keldysh parameter [15], γ, a number dependent on frequency, ν, work function, ϕ,and local (enhanced) field amplitude, E according to:

$$\gamma = \omega \frac{\sqrt{2m\phi}}{eE} \tag{1.12}$$

where m and e are the mass and charge of the electron, respectively. γ considers not only amplitude, but also frequency to include effects of the response time of the electrons. For $\gamma \gg 1$, the so called "weak field limit", effects to the potential barrier are negligible. Absorption of photons for over-the-barrier emission provide the only description for electron emission. Commonly, two or more photons are necessary to overcome the work function, giving this process the name "multi-photon ionization" (MPI), shown in Fig.(1.7a) [24]. For silver and gold, the work function requires electrons to absorb ~ 3 photons of light produced by Ti:Sapph lasers for MPI. Ionization has recently been reported in the literature for up to 9 photons from gold nano particles, although at the high fields required for 9 photon excitation ponderomotive forces complicate the simple picture presented in FIg. 1.7 [6]. Ionization such as this, by more than the minimum number of photons required, is generally referred to as "above threshold ionization" (ATI), depicted in Fig.(1.7b). For $\gamma \ll 1$, the "strong field limit", the oscillating field distorts the local potential barrier, suppressing and raising the work function for each full optical cycle. During the half-cycle when the work function is suppressed, tunneling of electrons into the vacuum states is possible for strong enough fields and allows electron emission via multiple interactions. Photo-induced tunneling describes the tunneling of electrons after absorption of one or more photons through the suppressed barrier, depicted in Fig.(1.7c). If thermal contributions are significant and bulk temperature rises, electrons heated above the Fermi level will similarly have higher tunneling probability and emit as thermionic emission. For time dynamic studies, this is a concern for times

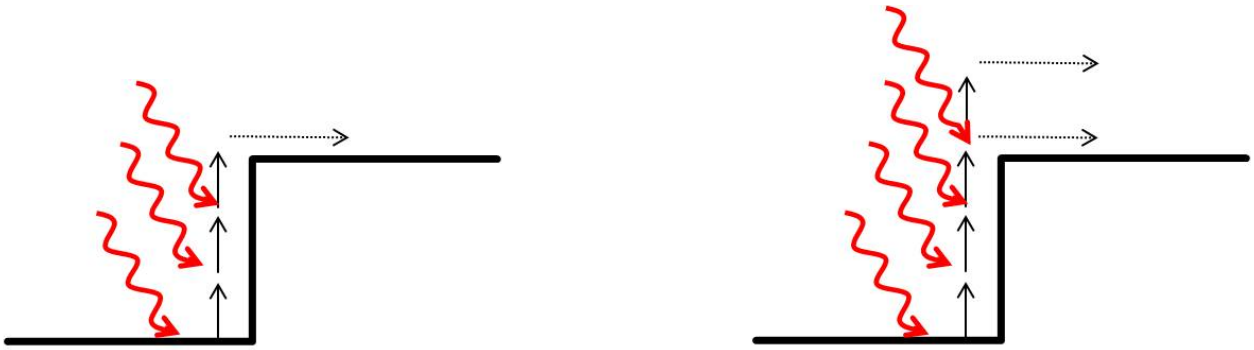

(a) Multi-photon ionization

(b) Above-threshold ionization

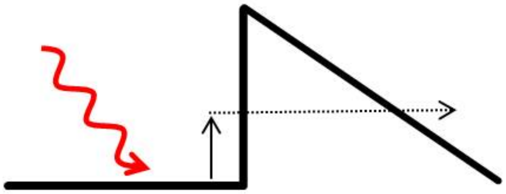

(c) Photo-induced tunneling

Figure 1.7: Electron emission with optical fields

longer than the electron-phonon scattering time, typically a few hundred femtoseconds. To investigate the effects of contributions to the emission current by tunneling, we'll begin with the simplest model of a static bias before expanding to include time dynamics. Field emission from metals in high applied static fields is known as Fowler-Nordheim field emission, named for the two authors to first describe the behavior in 1928 [8].

1.3.2 Time-independent Approximation of Fowler Nordheim for Optical Fields

Static Fields

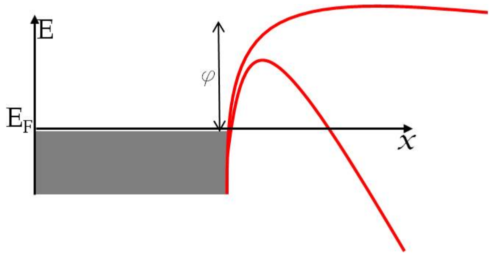

Figure 1.8: Fowler-Nordheim potential barrier.

In the original Fowler-Nordheim (FN) model, the potential is described by a rounded triangular barrier, rounded because of the image charge effect (Fig. 1.8). As the barrier is brought down by the DC field, the probability of electrons to tunnel from the Fermi energy level increases as the barrier wall thins. A 1-D tunneling probability is given by:

$$P(E_z) = \exp\left[\frac{2\sqrt{2m}}{\hbar}\int\sqrt{E_z - eFz - \frac{e^2}{4z}dz}\right], \tag{1.13}$$

where F is the applied field and the last term in the integrand corrects for the image potential. The total current density is found by integrating over the available electrons and their tunneling probabilities for their given energies, described by (1.14).

$$j_{total} = \int P(E)D(E)dE, \tag{1.14}$$

The result is [8]:

$$j_{FN} = \frac{a\,F_{DC}^2}{\phi}\ \exp\left[c\frac{(\phi)^{3/2}}{F_{DC}}\nu(F)\right], \tag{1.15}$$

Where $a = \frac{e^3}{8\pi h\phi}$ and $c = 6.83\,\mathrm{eV}^{3/2}\mathrm{nm/V}$ are FN constants, ϕ is the work function, and $\nu(F)$ is a correction term necessitated by the non-analytic form of Eq. (1.13) . In reference to the integrable triangular barrier, $\nu(F)$ corrects for the reduced work function height from the rounding of the barrier by the image potential term [26]. This result does not incorporate geometry considerations of the emitter, but has been shown to match well with experiments using tip-shaped emitters when the geometry is used to calculate the local field at the apex for the value of F_{DC} [1].

For the experiments reported here, the field is a result of an applied voltage on the emitter and F_{DC} is found by multiplying the $F(V)$ for an infinite plane by a geometry dependent enhancement factor. The field enhancement,$F_{DC} = \beta V$, is due to the lightning rod effect and for a tip with radius R, the enhancement factor, β, is given by:

$$\beta = \frac{1}{kR} \tag{1.16a}$$

$$k = 0.59(\theta)^{\frac{1}{3}}\left(\frac{x}{R}\right)^{0.13} \tag{1.16b}$$

where x is tip apex to collector separation and *theta* is the half angle of the spherical cap describing the area from which electrons emit. As can be seen in Eq.(1.16b), k is predominantly determined by this angle. $\theta \simeq 25^\circ$ gives $k \simeq 5$ for most geometries, derived from statistical measurements of tip emitters, assuming an approximately spherical tip apex[1, 26].

Optical Fields with Quasistatic Approximation

In the case of field emission from an oscillating optical field, the tunneling probability is a function of time as the field amplitude shakes the potential barrier in both directions within each cycle. In the regime of local fields that give a Keldish parameter $\gamma \simeq 1$ exact mechanism of electron emission can become unclear. The quasistatic approximation neglects this time dependence and relates the optical field, or enhanced (by χ) plasmon field, to its time averaged intensity, $F_{pl} \propto \chi\sqrt{I_\omega}$. In the case of both a static bias and plasmon field, the field determining the tunneling probability, P(E), is taken as a summation of the two, $F_{tot} = F_{pl} + F_{DC}$. In the a priori assumption of a FN behavior for tunneling in this total field, current density is then given as:

$$j_{pl} = \frac{a(F_{pl} + F_{DC})^2}{\phi} \exp\left[-\frac{c\,\phi^{3/2}}{(F_{pl} + F_{DC})}\nu(F)\right]. \tag{1.17}$$

Eq. (1.17) has been used to describe high energy electron emission seen from plasmonically enhanced nano particles [2, 10, 18, 24] as well as irregularly shaped gold tips [12]. This model, however, ignores a key property of the oscillatory behavior; described by a Floquet treatment, the electronic response of the metal will produce an electron wavepacket with energy $\hbar\omega$. Collectively, this charge density comprises the local plasmon, which can now tunnel from a reduced workfunction, $\phi - \hbar\omega$, of its own creation. With no incident radiation, this creates a fascinating picture of electron tunneling. If the tunneling electrons create the local field that allows them to tunnel, once emitted, the local field raises the barrier and effectively closes the door on its way out. This emission is strictly coherent with the plasmonic oscillation, which also mediates tunneling from lower energies.

To include the supply function of electrons in the excited state picture, reciprocity provides an elegant description of the charge density, σ, which can be inserted into Eq. (1.17) to calculate the final current density. The WKB tunneling probability remains the same as Eq.

(1.13), now with a work function given by $\phi_{Ex} = \phi - \hbar\omega$. If we approximate the promoted charge as a box distribution over energies with width Δ, integrating from E_F to $E_F + \hbar\omega$ gives a charge density, $\sigma_{Pl} = \hbar\omega\Delta$. This density can be written as,

$$\sigma_{Pl} = 2\,\epsilon_0 F = \Delta, \tag{1.18}$$

where F is now our F_{Pl} of Eq. (1.17). From Eq. (1.18), we can solve for Δ, which is then a constant for the integral of Eq.(1.14). Finally, we have,

$$j_{E_{F+1.5eV}} = \frac{2\epsilon_0\, F_{Pl}\, e\, d}{\hbar\omega} \int\limits_{\phi}^{\phi+\hbar\omega} \exp\left[-\frac{E}{d}\, dE\right], \tag{1.19}$$

with

$$d = \frac{\hbar}{2\sqrt{2m_e}} \frac{F_{Tot}}{\sqrt{\phi - \hbar\omega}}, \tag{1.20}$$

The resulting expression is:

$$j_{pl} = \frac{\epsilon_0\, e\, F_{Pl}(F_{Pl} + F_{DC})}{\omega\sqrt{2m_e\,(\phi - \hbar\omega)}} \exp\left(-\frac{c\,(\phi - \hbar\omega)^{3/2}}{(F_{DC} + F_{pl})}\nu(F_{\phi-\hbar\omega})\right) \tag{1.21}$$

Eq. (1.17) and (1.21) provide two functional forms, differing by a power of F_{DC} in the prefactor, to compare to data and determine if a best fit is clear and what conclusions can be made about the plasmonic fields at the apex.

Chapter 2

Fabrication of Plasmonic Probe Tips

2.1 Traditional Electrochemical Etching

Efficient surface plasmon propagation requires a smooth surface, free of defects from which scattering can occur. For most probe tips surface structure away from the apex is of little concern. It is only the apex shape that determines its effectiveness. For our purposes, the surface between where the plasmon is excited, here the grating, and the apex is as important as the apex itself.

Typically, tips made of gold or silver are electrochemically etched at the interface of the etching fluid. For this technique, we start with rough tips electrochemically etched from either gold or silver wire of 500 μm radius. The wire is first oven annealed at $750°C$ with a 2 hour cool-down. For silver we follow a method similar to [33], using a solution of 100% methanol, 28% NH4OH, and 30% H202 in a 1:1:1 ratio and an etching voltage of 15 - 20V. For gold we follow the method of [22] with a 1:1 solution of 37% HCl and 100% ethanol and an etching voltage of 2.4V. Both processes are terminated with a cut-off circuit that shuts off the etching bias at the break-off point to reliably produce tips with apices of <100 nm.

With focus of these processes predominantly on the final apex radius, little work has been done in making the overall surface free of the defects created by the etching. Etching of silver in particular results in large facet structures and defects of the order of a few microns or more.

2.2 Focus Ion Beam Nanofabrication

2.2.1 Annular Ion Beam Cleaning

To improve the surface smoothness of our probe tips, we used a focused ion beam (FIB) of gallium ions in a FEI Quanta 3D SEM/FIB system to remove gross features after the electrochemical etching process. This FIB functions as described in [9], producing a beam of Ga ions accelerated at an adjustable 3-20kV. Mounted vertically, the tip is collinear with the electron beam and 52° relative to the FIB source. FIB cleaning was done in one of two ways. Initially, we followed a method similar to [29], using a shower of ions in a collinear geometry to knock off protrusions from the tip. This was done with caution, as metals such as silver and gold accumulate pitting along the crystalline facets as the ion beam etches head-on into the material. This effect, sometimes referred to as "curtaining," is more pronounced if multiple masks of decreasing size are used to etch away bulk material. This can leave behind ridges with depths on the order of microns, seen in Fig.2.1. To avoid this effect, FIB etching in this manor was used to remove only material on the order of a few hundred nanometers in depth.

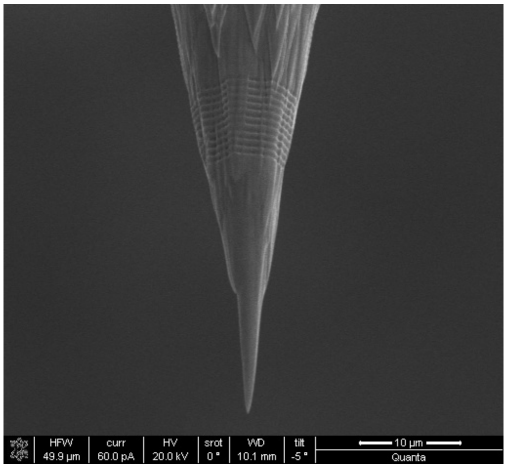

Figure 2.1: “Curtaining” defects seen on annular etched Au tip.

To preserve the sharpness of the tip apex, annular masks for tips with small cone angles, $\sim 7°$, often resulted in rough structures remaining on the last 5-10 µm.

2.2.2 Lathe Ion Beam Etching – A new approach

To provide an essentially defect free surface for the entire ~ 30 µm length of the probe tips, the FIB was used in a second method, adapted from micromachining techniques used in lift out (LO) probe production methods as well as microcircuit production [Cite]. In this novel method, the FIB is used instead in a perpendicular geometry, where material is etched by the edge of the ion beam with a 0° incidence angle relative to the normal as the tip is rotated. Bulk material is etched in this case, however curtaining does not occur as material is only removed at grazing angles. The ion beam etches material in a manor analogous to the knife edge of a lathe tool. Similar to methods summarized in [20], etching is controlled by scripts written for the microscope's software and is, in large part, automated for commercial FIBs controllable by software commands.

This etching is done once the tip has been electrochemically etched to any apex radius $<\sim 500nm$. These rough tips are then mounted vertically in a tip holder that sits close to the FIB chamber's center. The FIB is used both to image and to etch in this arrangement. We found an accelerating voltage of 10 kV and 2 nA of current to produce a beam that etches in a reasonable amount of time while minimizing ion implantation both in etching and imaging. Because we use the edge of the beam to etch material, absolute beam size is important mainly for imaging resolution.

To etch in this way, we define a polygon etching pattern with the inner edge forming the desired half angle of the final tip. The polygon acts as our 'blade.' The pattern is fixed on the ion beam image quadrant such that inner edge, and therefore, final apex, will be at the center of the image Fig. (2.2a). The tip is brought into focus on the image with a field of view large enough such the window is twice the length of the desired tip etching length, keeping in mind the 52° angle of the FIB. For us, this is in general $\sim 80\mu$m, or 1500-3000x magnification. The rough initial tip apex is likewise placed at the center of the image and a cut is made. With the etching pattern fixed, the tip is then rotated about its axis by 10° and re-centered before a successive cut is made. This is repeated for a full 360° rotation.

Making successive cuts as the tip is rotated about its axis is analogous to the mechanism of a lathe. These steps are illustrated in Fig.(2.2). When starting with a tip whose initial cone angle is much bigger that that of the blade, we found it was better to first etch a tip using a wider angled polygon and repeat the process with the desired angle. For tips whose initial apex is irregular, without a clear apex at all rotation angles, we found it best to make 3-4 large angle cuts around the tip to form an approximately symmetric point the best re-centering of the tip image at all angles. Note, however, a larger initial radius will require more etching time. For reasonable initial radii ($< 3\mu$m) the process takes $\sim$ 4hrs.

The precision of the process was further increased by automation using the FIB operating software's ability to match a captured image with a stored image. With this ability, the entire process was programmable, adapted from the technique developed by [Naval paper]. With a stored, cropped image of the apex, the actual tip apex could be matched after each

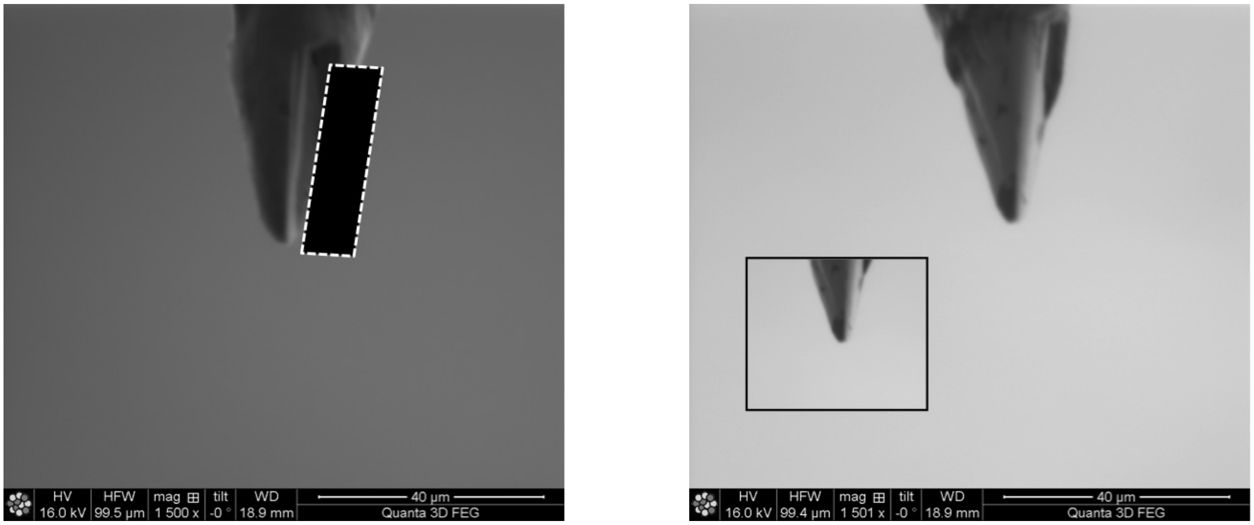

(a) Tip image with "blade" pattern, shown as polygon with dashed, white outline.

(b) Tip after first few etched cuts with example of matching image used for re-centering of tips after each cut and subsequent rotation step.

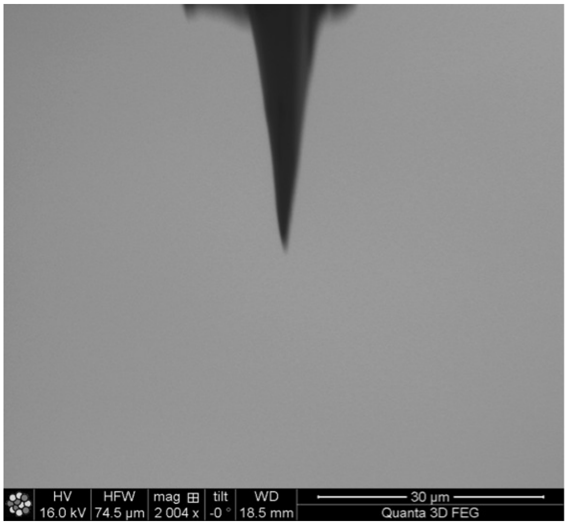

(c) Tip as seen by FIB image before final cut.

Figure 2.2: Lathed FIB tip in three stages of the fabrication process.

rotation and placed more precisely at the center of the image, where the blade corner is fixed. An example of this matching image is shown inset in (Fig. 2.2b). Although the stored image must be updated every 5-10 cuts to assure accurate matching as the tip takes shape, the majority of fine control of the process is optimized by the software.

Fig.(2.3) shows SEM images of electrochemically etched silver (2.3a) and gold (2.3b) tips

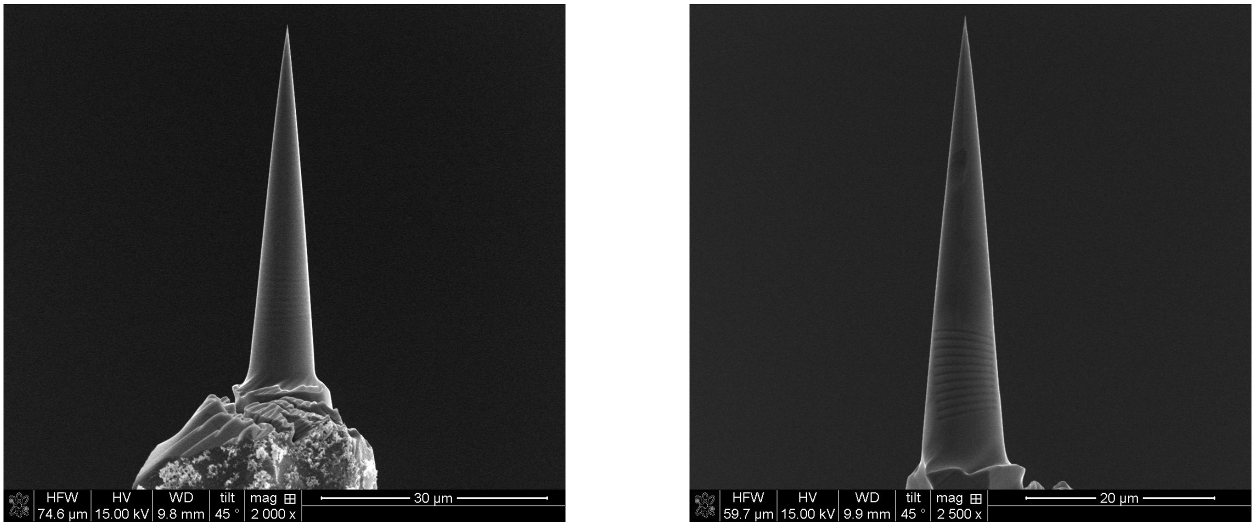

(a) Final Lathed Tip, Silver (b) Final Lathed Tip, Gold

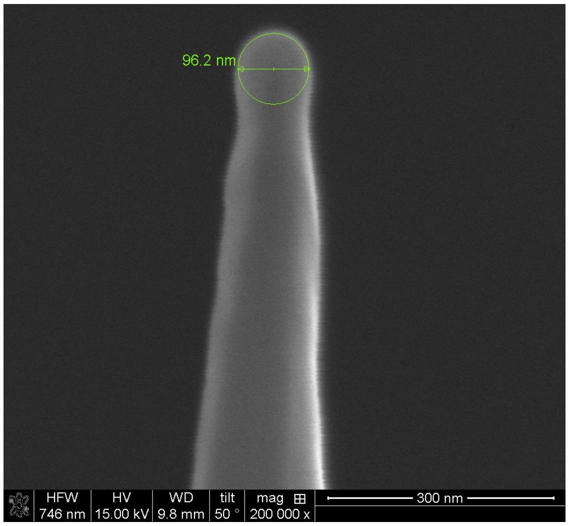

(c) Tip apex.

Figure 2.3: Final lathed FIB etched tips

after the FIB procedure. After the procedure the silver and gold tips have an apex radius of $\sim 40\,\mathrm{nm}$ (Fig. 2.3c) and $\sim 25\,\mathrm{nm}$ nm, respectively. They both have cone angles of $\sim 8°$. Unlike the annular method of FIB etching, the cone angle is finely controlled, defined by the "blade" angle relative to the tip axis, and not dependent on beam focus. In our experience, a defocusing or misalignment of the beam of just a few microns for an annular mask at the final stages of etching can also easily destroy the apex. For the lathe orientation, the only limitations on minimizing this angle are structural, with smaller cone angles producing tips that are too delicate to transport. For studying the propagation of surface plasmons on these tips, a smaller angle allows for a longer adiabatic propagation length [Stockman].

The final surface roughness depends on the depth of the finishing cuts if crystal facets exist close to the surface, as well as the tolerance of the image matching function. Irregular facets were minimized with annealed wire. At most, remaining structures on the surface are in the 10's of nm and sparse, easily avoided in SPP applications with small rotations of the tip.

Chapter 3

Experimental Observation of Plasmons on Probe Tips

3.1 Experimental Set-Up

3.1.1 Electronics

The probe tip is housed in a high vacuum chamber with a pressure of 10^{-6} Torr. The tip is negatively biased with DC voltage relative to a .25" diameter brass collecting rod. The separation between the tip and collector is held constant, between 100 - 300 um for each experiment, far outside the tunneling regime. As shown in Fig. 3.1, electrons are collected by the brass rod and sent to an Ithaco current preamplifier. Signal is then sent to both a lock-in detector locked to the frequency of the optical chopper for AC measurements and a SRS boxcar averager for simultaneous DC measurements.

For current measurements taken as a function of applied DC bias in this configuration, lower limits of noise are of the order 0.1 pA, or 1 electron per 100 pulses of our 80 MHz. In

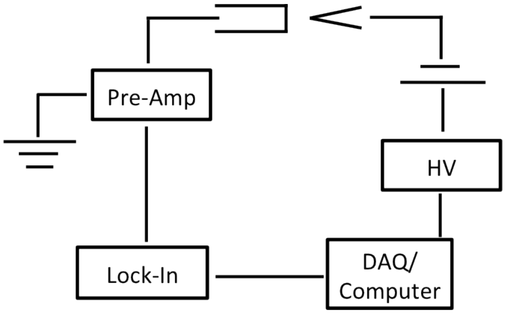

Figure 3.1: Circuit diagram for current measurements.

general, field emission current measured up to $\sim 1\,\text{pA}$, or 1 electron per 10 pulses. Therefore, measured field emission produced signal-to-noise ratios of $\sim 10:1$. This was limited by the applied DC extractor fields needed to measure plasmon dependent current (greater than $0.1\,\text{pA}$) relative to the fields needed to see pure DC emission, fields under which tips were likely to incur damage ($\sim 5\,\text{nm}$). This is discussed in further detail with experimental results.

3.1.2 Optics and Full Experimental Picture

SPPs are launched towards the apex on the tip by illuminating the etched grating with 20 fs pulses from a Ti:Sapph laser with a central frequency of $\sim 790\,\text{nm}$ and repetition rate of 80 MHz. The pulses are pre-compensated with negative chirp using a chirped pulse compressor (CPC). The 80 nm of bandwidth in each pulse are given -1300fs^2 to account for acquired chirp of the optics. Using autocorrelation measurements of the frequency doubled signal through a BBO crystal yields pulses of $\sim 20\,\text{fs}$. The full experimental setup is depicted in Fig. 3.2. The beam is sent through a chopper and then split into two arms, one with a delay stage, and recombined as an interferometer for time dependent measurements. Finally, the beam is sent to a half wave plate (HWP) followed by composite lens objective with NA 0.16 by reflection from a 50/50 beamsplitter and focused on the grating through a 1mm thick sapphire window on the vacuum chamber housing the tip. In this configuration, the tip and chamber are held stationary while the objective is controlled in three dimensions with piezo-actuated stages.

With the positioning of the laser on the tip controlled by the movement of the objective, we use the independently controlled movement of the steering mirrors to displace the 3mm beam on the 6mm objective to tune the incidence angle of the beam relative to the grating. These relative diameters and the numerical aperture of the lens allow for an incidence change ±5 deg. Because the tip is manually mounted in the vacuum chamber, this control allows fine tuning for optimal coupling.

Radiation from the tip apex and backscattered light from the grating are collected through the objective, pass through the beamsplitter and the image is magnified with a tube lens as a 60x microscope. An iris in the image plane allows for selective imaging of the apex, blocking the specular reflection from the grating. The final image is sent either to a Sony camera for gross adjustments in aligning or an Andor CCD for numerical analysis and precise optimization.

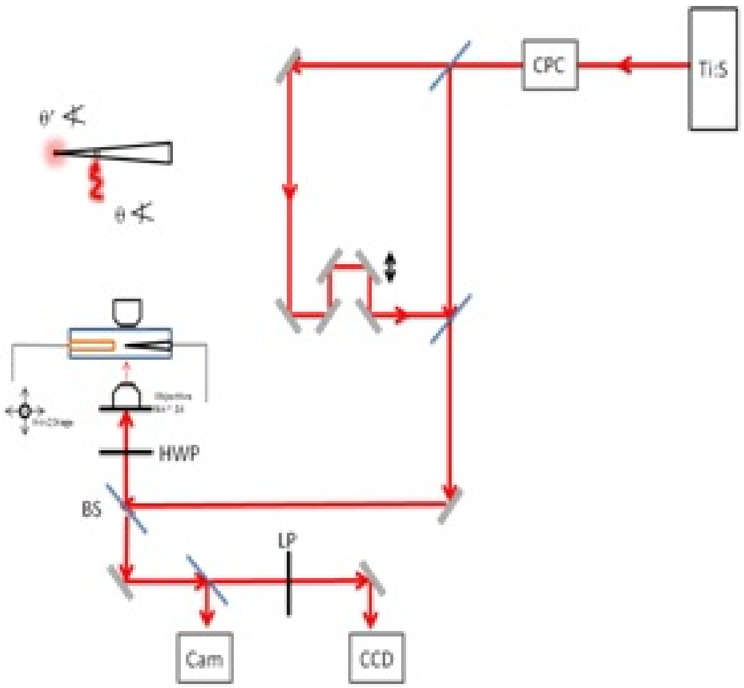

Figure 3.2: Experimental setup. Pulses from a Ti:Sapph laser are pre-compensated for chirp and chopped for amplitude modulation at 400Hz. The beam is sent to the chamber with a 50/50 beam splitter and focused onto the probe tip grating through a .16NA objective whose position is controlled in three dimensions with piezo-actuators for precise coupling optimization. Backscattered light through the objective and beam splitter are sent through a tube lens for 60x magnification before imaging in both a camera and CCD.

Light measurement procedure for all tips

The intensity of this light scales linearly with SPP coupling efficiency at the grating and provides a reliable verification of SPP coupling and a method for optimization [25]. A multitude of spatial parameters determine the coupling efficiency for an incident beam on a grating [23]. These parameters include the spot size (focus), positioning on the grating, incident angle, and polarization, each of which are adjusted independently and their effects monitored by the light imaging from our 60x microscope. From the CCD image of the 60x magnified light from the tip, the area surrounding just the apex is isolated for intensity measurements. Fig3.3 shows an example of a CCD image of the apex radiation. The outline of the iris blocking the specular reflection in the image plane can be seen, as it also blocks the scattered light from the chamber. The red box indicates the area over which we integrate to assign an apex radiation intensity.

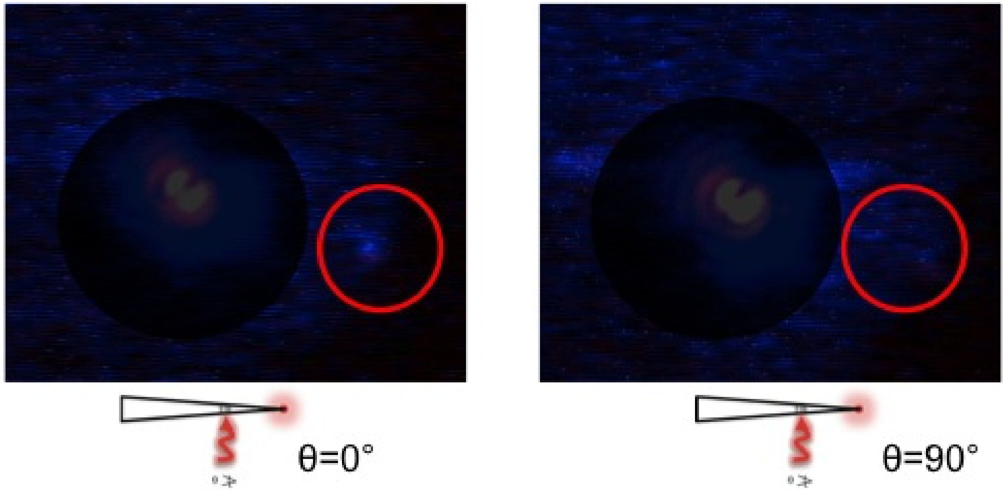

Figure 3.3: CCD image of apex radiation

We etch our gratings on the probe tips with grooves cut perpendicular to the tip axis, such that momentum matching launches the SPP towards the apex. Maximum coupling, and resulting brightness of apex radiation, will occur for incident light polarization parallel to the tip axis, and therefore perpendicular to the grating. We verify the linear dependence of the apex radiation intensity vs. incident polarization to ensure launching. This dependence is shown for a tip smoothed with the annular FIB method Fig.(3.4) with the fitting function $a+b\cos(\theta+c)^{(d)2}$ overlaid (in red). The clear $\cos(\theta)^2$ dependence sits on top of a background of scattered light from the chamber. A direct laser power dependence measurement similarly shows linear behavior, as shown in Fig.(3.4a).

Each tip is mounted in the vacuum chamber manually and so the 30μm probe end of the tips will each be aligned slightly differently relative to the chamber and optics. We optimize the incident laser on the grating for coupling to produce the most radiation from the apex. Optimal positions of the laser spot were general near the center of the grating, as was expected to illuminate the largest area of the grating. With the focus $\sim 2-4\,\mu$m from the focal point, the laser spot size illuminates multiple grooves of the $\sim 10um$ length grating for best coupling. At the focal point the spot size is 2 µm and we estimate $\sim 5 - 10$µm spot size near optimal coupling. Once optimized, we verify the linear power dependence of the incident field, as shown in Fig. **??**, and intensity is then compared to all subsequent current measurements to assure correlation.

It is worth noting that SPP that arrives at the apex depends not only on coupling at the grating, but also on losses as it propagates to the apex. Minor deviations in propagation paths that may arise from irradiating different areas of the grating were found to influence the final field delivered to the apex, but not the linearly dependent apex brightness. Because these movements are smaller than the fall off of apex intensity with position, the polarization dependence governs the apex brightness, as is seen Fig. 3.4b.

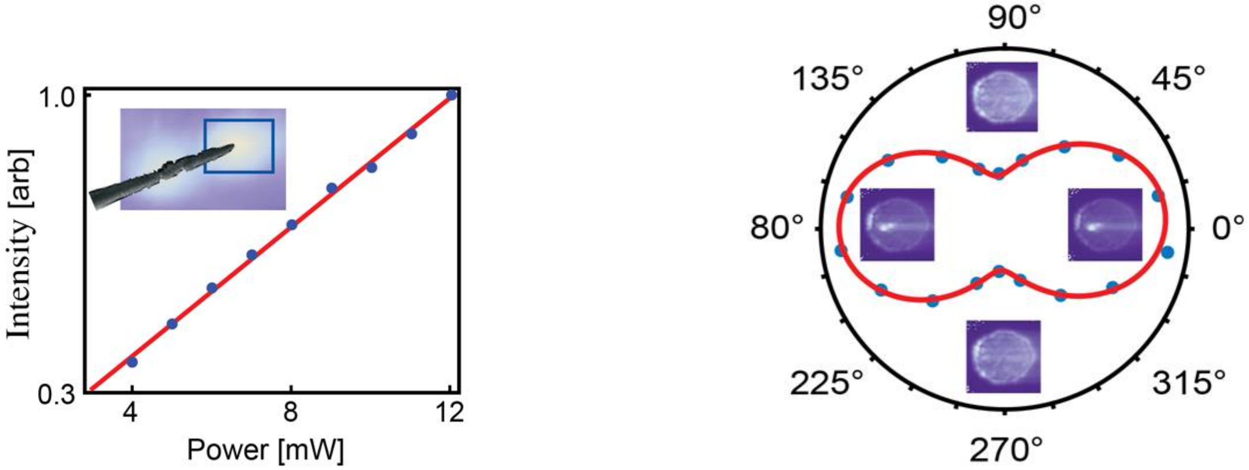

(a) Power dependence of apex radiation on incident beam.

(b) Polarization dependence of apex radiation on incident beam.

Figure 3.4: Spacial dependence of incident beam for apex radiation from coupling and super focusing

Optimization of the beam's incident angle, in our experience, was the most vital factor for efficient coupling and required somewhat more care in measuring the apex brightness. Because the image is formed with the focusing objective, changing the tilt changes the amount of specular reflection chamber scattering that can fall within the objective's acceptance angle and therefore the amount of background light. Normalization of intensity data cannot be done for the data set as a whole. Adjustments to the tilt also minimally move the beam and require fine adjustments in x-y-z to re-optimize. For each tilt angle measured two images of the apex were recorded, one with incident polarization parallel to the tip axis, where coupling is maximum, and another perpendicular where coupling is minimum. Using the difference of the integrated intensity values of the two images provided proper background subtraction for each measurement. Fig.(3.5) shows these values vs. incident angle.

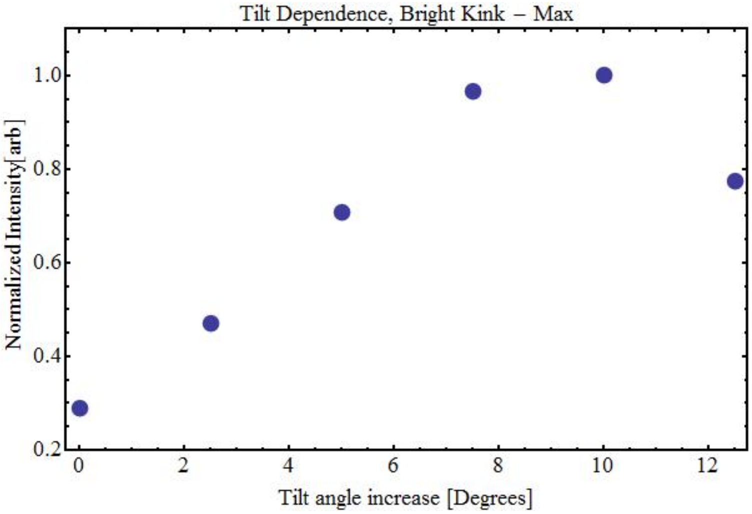

Figure 3.5: Incident laser angle dependence relative to tip-axis normal.

3.2 Measurements and Analysis of Plasmon Driven Currents by Fitting Models to IV measurements

As discussed in Chapter 1, direct irradiation of the apex of a probe tip leads to field emission that can be collected with small bias fields. Such emission can occur on sharp asperities of the tip, not necessarily at the apex. This was most clearly demonstrated by measuring emission current as a function of x-y position of the incident laser on the tip. Using a DC bias of $\sim 20V$ and average laser power of 9 mW a current map, which is superimposed on the SEM image of the tip in Fig. 3.6, tracks the asperities on the surface of the tip. Direct irradiation of such asperities typically produced measurable current in the range of 1 - 10 pA with incident average power of $\sim 2 - 10$mW, depending on the roughness and material.

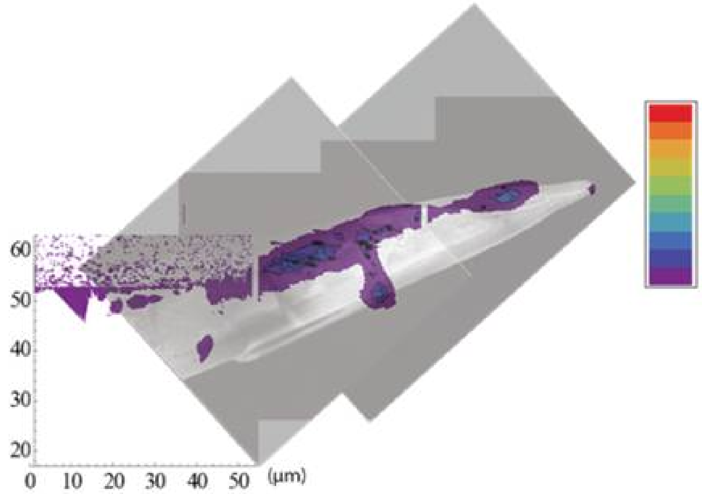

Figure 3.6: Map of current amplitude as incident laser is 2D raster-scanned over a silver tip with asperities.

Field emission from directly irradiated asperities is characteristically unstable: the current fluctuates on the time scale of seconds, polarization dependences are transient, and current fluctuations as large as two orders of magnitude are observed upon spatial adjustment of the incident beam by just a few hundred nanometers. These characteristics indicated local field enhancement in the crevices and features of the asperity were changing, possibly by thermal heating and melting. Although these rough areas provided a less straightforward picture of the ideal conical super focusing, for the tips whose surface was otherwise mainly smooth and had structures sufficiently close to the apex, they themselves have local enhancement properties similar to that of an apex and potentially act as local emitters or cluster of emitters upon the arrival of the SPP.

Reliance on polarization dependence alone to identify coupling to the grating and therefore field emission driven by the SPP can be misleading. One such tip, shown in Fig 3.7a, produced measurable, polarization dependent current with the laser incident on the grating.

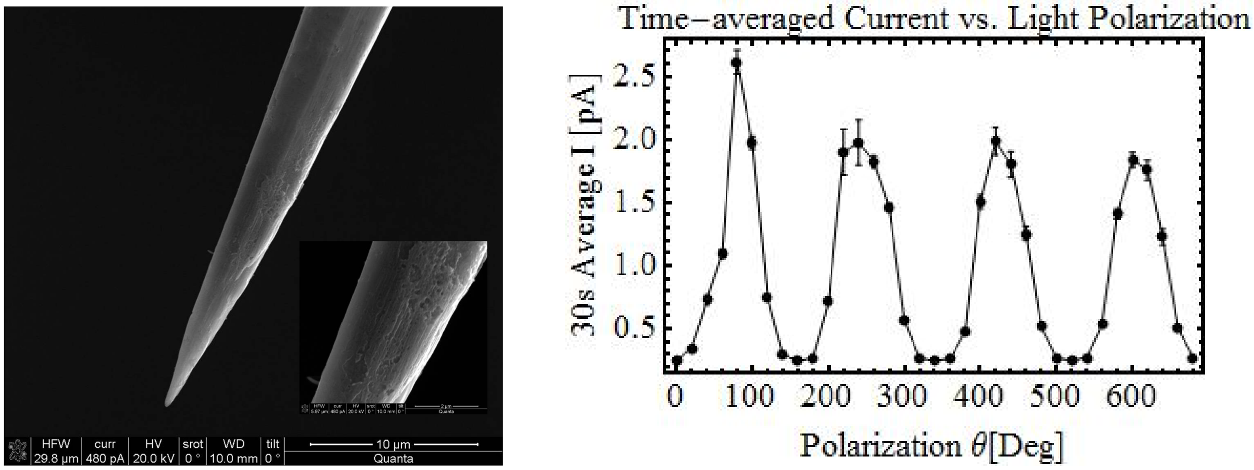

(a) Silver tip with area of asperities near apex, asperities shown inset.

(b) Time (30 s) averaged current t vs. polarization angle.

Figure 3.7: Current from tips with asperities.

With a relatively large radius of ∼80 nm from which no light could be collected, it seemed plausible a single nm-sized asperity within the rough area could produce current, but be too small to produce measurable radiation. Time-averaged current as a function of polarization for this tip is plotted in Fig. 3.7b. When the tip was imaged with an SEM after measurements, clear damage to the grating was evident, preferentially along the groove edges, shown in Fig. 3.8b. With no correlated radiation from the apex there was insufficient evidence to support the hypothesis of SPP driven current from the asperities. With this new insight, current measurements from grating-coupled tip excitation were only taken once coupling was verified and maximized. For the tips reported here, SEM images after measurements were used to confirm no local damage occurred at the grating.

In the case of direct irradiation of a singular apex, it was typically necessary to apply an extractor field to see laser induced FE. By increasing the DC bias on the tip, we lower the tunneling barrier to supplement the plasmonic field at the apex to reach detectable field emission. This same holds for the case in which the laser is only incident on the grating and the FE the apex is from the super focused SPP. Superfocusing ensured by the observation of radiation emitted at the tip apex when irradiating the grating. Once coupling

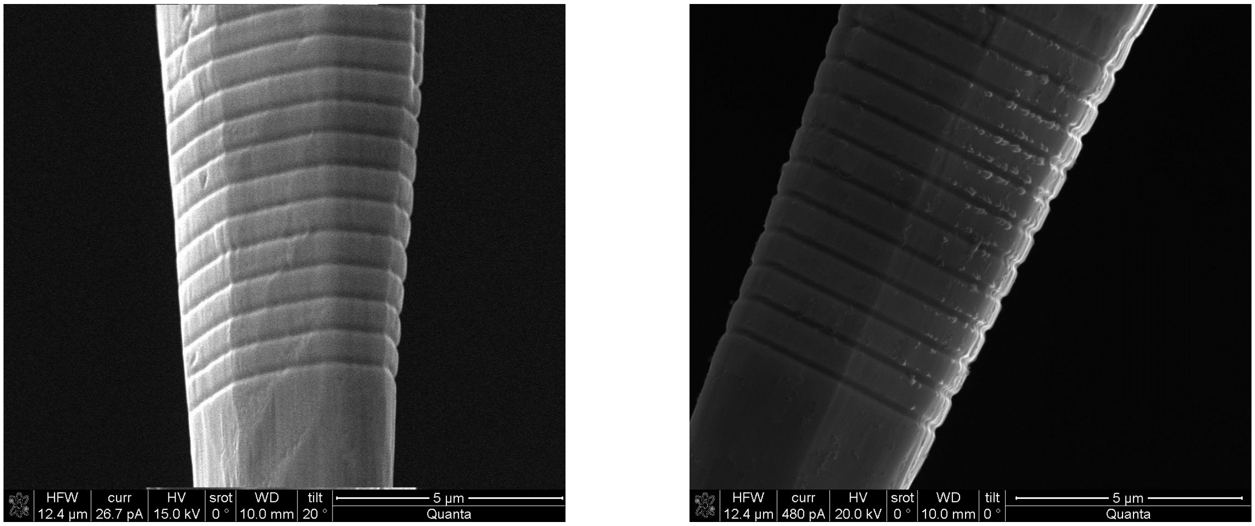

(a) SEM image of grating on silver tip before current measurements

(b) SEM image of grating on silver tip after current measurements showing clear areas of local damage, preferentially located near the edges of grating grooves

Figure 3.8: SEM images of etched grating before and after measurement.

is verified and maximized, we look for induced current with the extractor field. Given the tip-to-tip variation of the threshold for observable DC or laser induced emission, we adopt the experimental approach whereby we first determine the DC induced FE curve of a tip, and subsequently record the light induced FE as we scan the bias without exceeding this threshold. Systematic results are obtained from data sets recorded on several tips. I will present this data here for three tip results and discuss their analysis and the extracted information.

Current measured with the described extracting field results from tunneling of electrons into the vacuum with contributions from both AC and DC fields. Typically, current of this nature is modeled by a Fowler Nordheim based picture, with adaptations to the electron supply function used to account for electron-hole excitation[3, 25, 26, 30, 31]. These electron-hole models do not include the dynamics of the plasmon, i.e. coherent collective oscillations of the surface charge density which controls the tunneling barrier. With no incident field in the experiments reported here, it is only this wavepacket with energy $\hbar\omega$, that creates the local field.

For the quasistatic approximation, we want to see if measurements of current as a function of the static field, with the addition of the local plasmon field, display clear characteristics of either tunneling primarily from the Fermi level (Eq.(1.17)), or from excited platoons (Eq.(1.21)). The voltage dependent current data was fit to Eq. (1.17) and (1.21), given as:

$$j = j_0 + a\,(F_{DC} + F_{pl})^2 \exp\left(-\frac{c\,\phi^{3/2}}{(F_{DC} + F_{pl})}\nu(F)\right), \tag{3.1a}$$

$$j = j_0 + a\ F_{pl}(F_{DC} + F_{pl}) \exp\left(-\frac{c\,(\phi - \hbar\omega)^{3/2}}{(F_{DC} + F_{pl})}\nu_{1.5eV}(F)\right). \tag{3.1b}$$

F_{DC} is given by $F_{DC} = \frac{V_{DC}}{kR}$, where R and k are the tip radius and geometric enhancement term given by (1.16b), respectively, where k is calculated for each radius with a distance of 100 µm. j_0 is the noise floor and $\nu(F)$ and $\nu_{1.5eV}(F)$ are correction functions of the total local field for the given work functions, ϕ, which is either 4.5 eV for silver or 5.1 eV for gold [14, 16]. The variable a is left as a fitting parameter for both equations, where the final area of emission from the tip, $A_{j(FN)}$ and $A_{j(1.5eV)}$, are found by dividing the value of a by the constants from Eq. (1.17) and (1.21), given as,

$$A_{j(FN)} = a\,B = a\left[\frac{8\pi h\phi}{e^3}\right] = \frac{\sim 0.04}{\phi}\mathrm{pA\,V^{-2}}, \tag{3.2a}$$

$$A_{j(1.5eV)} = a\,B = a\left[\frac{e\,\epsilon_0\,\Omega_{Rep}}{\omega\sqrt{2\,m_e\,\phi}}\right] = \frac{\sim 1.07\,\mathrm{pA\,V^{-2}}}{\sqrt{\phi}}. \tag{3.2b}$$

m and e are the mass and charge of an electron, respectively, and ϵ_0 is vacuum permittivity. The ω in the denominator is the plasmon oscillation frequency, while $\Omega = 76\,\mathrm{MHz}$ in the numerator is the repetition rate of the oscillator. Both (3.1a) and (3.1b) are fit to the complete sets of measurements taken for three separate tips and the results are compared and discussed.

3.2.1 Chemically Etched Silver Tip

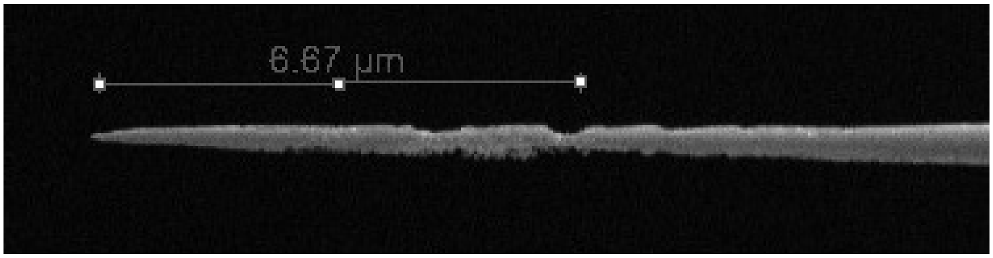

Figure 3.9: SEM image of Ag tip with area of asperities near apex.

For the tip made with the annular FIB cleaning, shown in Fig.3.9, the majority of the surface was smooth while multiple features and asperities remained near the apex. The structures collectively in this case showed clear, coupling dependent radiation emission and verifiable nonlocal current. We measured the laser induced current as we increased the DC bias from 0 V to 750 V, below the 800 V static FE threshold of this particular tip. With incident power on the grating just below the local damage threshold ($\sim 20mW$ here) field emission current was measurable only in bias ranges $> 500\,\mathrm{V}$. With multiple rough structures so close to the apex, including the notch seen radiating in Fig 3.4a (inset), scattering losses may have been a dominant factor.

Examples of raw data with fits to both models for $R = 60\,\mathrm{nm}$ and irradiation power of 10 mW (peak field of 0.34 V/nm) at the grating, are shown in Fig. 3.10. Incident field strength was limited by the damage threshold at the grating and the superfocusing efficiency of this tip could not deliver a plasmon field at the apex that would not allow for safe measurements at the high fixed DC bias required to see current above the $\sim 0.1\,\mathrm{pA}$ noise. At such a bias, $\sim 600 - 700\,\mathrm{V}$ in this case, fields are close to the SFE limit and tips are prone to arcing and macroscopic melting after extended periods of time. This first measurements was taken at 10° rotation increments of the half waveplate, equating to 20° increments in polarization angle; examples of raw data and their fits for two such angles are presented in Fig. 3.10.

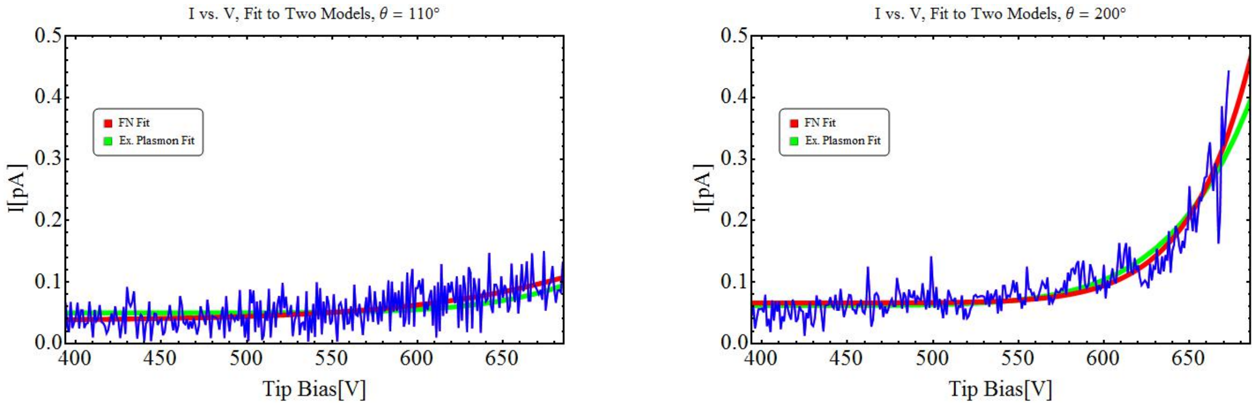

(a) Raw data (blue) and fits to both models for $\theta = 110°$.

(b) Raw data (blue) and fits to both models for $\theta = 200°$.

Figure 3.10: Example of raw data and fits, $\theta = 110°\,, 200°$

Results display a clear polarization dependence of the current coincident with that of the apex radiation intensity, but the data can be fit equally well to both models. Differentiating between the two models requires careful assessment of the extracted fitting parameters from the two function and what they imply for the underlying physics. Of importance to note first is the origin of R values used here, as well as in discussions to follow. With a fixed distance between the tip to collector, the tip radius, R, defines the scaling factor, β, to translate applied bias to local static field values. Fits to measurements are made for a complete set of sequentially taken bias dependencies for increasing polarization angle. Only values for which a global fit could be made are reported, with higher tolerance allowances for measurements containing little or no current above the noise within a given set.

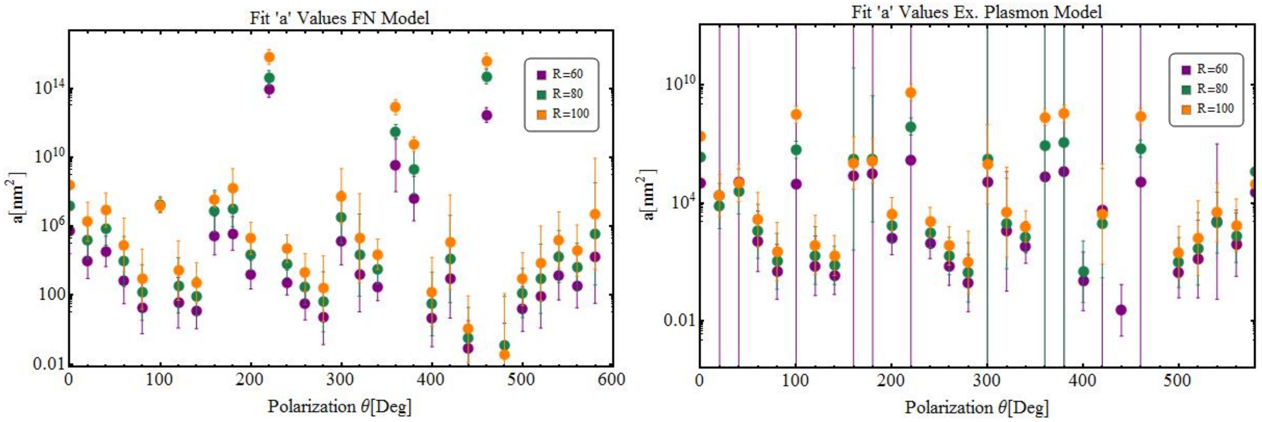

(a) Resulting values of a values vs. polarization angle from fits to the Fermi model, Eq. (3.1a), for 3 values of $\beta = kR$ for $R = 60\,\text{nm}, 80\,\text{nm}$, and $100\,\text{nm}$

(b) Resulting values of a vs. polarization angle from fits to the Excited level model, Eq. (3.1b) for 3 values of $\beta = kR$ for $R = 60\,\text{nm}, 80\,\text{nm}$, and $100\,\text{nm}$.

Figure 3.11: a values vs. polarization angle from fits to both models for current.

Given the rough surface of the apex, multiple irregular structures could be contributing to the current here. If each small structure acts as a single emitter, measured current would be comprise of the integral contribution from each smaller structure over the (large, compared to the quoted radii) apex surface that is rough, producing large values for emission area. Factoring out known constants in each functions pre factor, as described by Eq.'s (3.2), gives the average areas in table 3.1.

From the fit values of a, we can immediately see the large errors of each value and low precision across the set for both functions. F_{Pl} and a, and the limited dynamic range of the measurement, the pre-exponent a is indeterminate. Note that in principle a is only a function of the area, which should be constant for the set. Accordingly, if we choose a value from the data set and refit the curve fits to a function with only one free parameter, we would expect, at least, trends to emerge with better statistics. Note, the DC field is strongly determined by the chosen radius of curvature, and assumed model for local enhancement. With the assumed choice, the extracted value of the plasmon field is not well determined, since it is much smaller than the DC field and can be neglected in the exponent. In both models we see

Average A, Ag Tip (Elec. etched)		
R(nm)	$A_{FN}(\mathrm{nm}^2)$	$A_{j(1.5eV)}(\mathrm{nm}^2)$
60	1.38×10^5	1.34×10^5
80	2.90×10^6	1.18×10^6
100	2.80×10^7	6.95×10^5

Table 3.1: A values calculated from a used for 1-parameter fits. These are average values of the median 30 percent of 2-parameter results to include only those values with the most statistically meaningful fitting results.

that the extracted areas are ~ two orders of magnitude larger than what would be expected based on the assumed value of R. The analysis suggests that the tip behaves as a large area emitter, i.e., many asperities contribute to the observed emission. This is consistent with the SEM image and the observed distributed light emission.

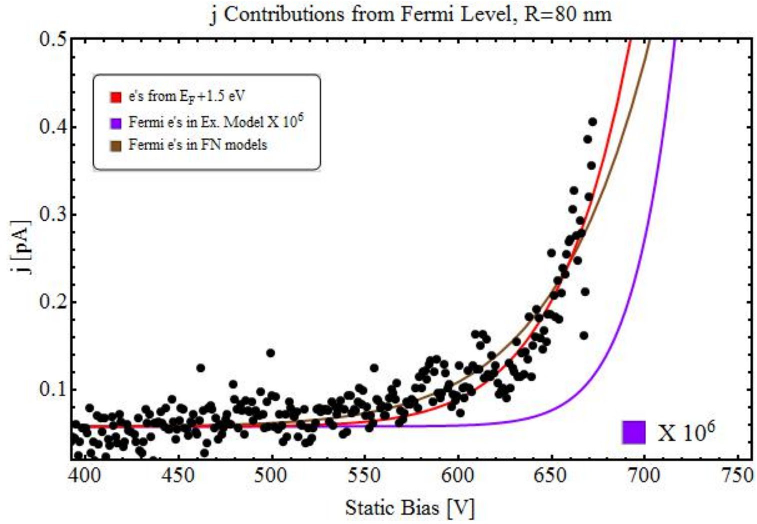

Figure 3.12: F_{pl} values vs. polarization angle given by both models using radius, $R = 80\,\mathrm{nm}$.

Comparing the two models directly, Fig .3.13 shows extracted F_{pl} vs. θ from 1 parameter fits to data (3.11) using values of a as reported in Tab. 3.1. There is approximately an order of magnitude difference between the two sets of values. Field strengths approximate to even the maximum value found from the excited state are then an order of magnitude smaller than the total fields produced by the static bias, whose smallest values associated with producing current for this radius are $\sim 2\,\mathrm{V\,nm^{-1}}$.

Because these plasmon fields play essentially no role in the exponential dependence, their predominant role in this regime is in populating the plasmon wavepacket density to tunnel to from above the Fermi energy. To be careful, we must also consider contributions to the total current from the fermi level that tunnels out with excited charge density. Eq. (3.1a), for FN tunneling from $E = E_F$, is plotted in Fig. 3.13 using the same $R = 80\,\mathrm{nm}$, but a is now given by $a = b\,A_{j(1.5eV)}$, where b is the constant of Eq. (3.2a) for the FN equation. This function is scaled by a factor of 10^4 to be plot with the fitted functions for current from the both models for the same apex radius, demonstrating no significant contribution. Data from the set corresponding to the field values used in the functions is also shown.

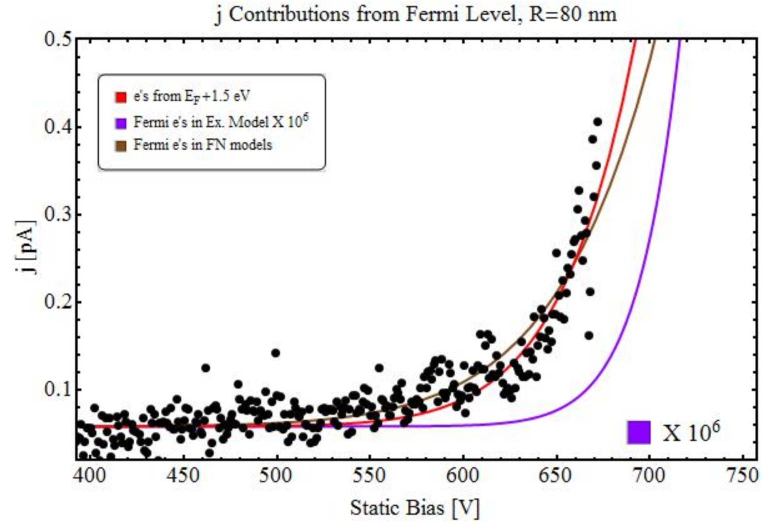

Figure 3.13: Calculated current from Fermi tunneling in the excitation model and that from each model alone for relevant range of applied DC voltage. $R = 80\,\mathrm{nm}$, $A_{j(1.5eV)} = 1.18 \times 10^6\,\mathrm{nm}^2$

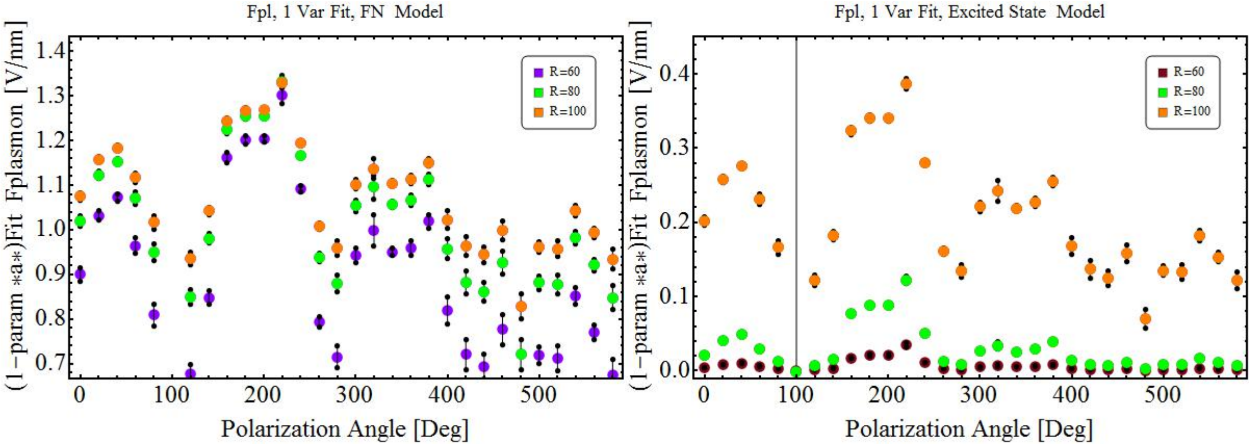

(a) F_{PL} vs. polarization angle from one-parameter fits to the Fermi model, Eq. (3.1a), for 3 values of $\beta = kR$ for $R = 60\,\mathrm{nm}, 80\,\mathrm{nm}$, and $100\,\mathrm{nm}$.

(b) F_{PL} vs. polarization angle from one-parameter fits to the Fermi model, Eq. (3.1a), for 3 values of $\beta = kR$ for $R = 60\,\mathrm{nm}, 80\,\mathrm{nm}$, and $100\,\mathrm{nm}$.

Figure 3.14: F_{Pl} values vs. polarization angle from fits to both models for current.

The local plasmon field varies with a $\cos^2(\theta)$ dependence, seen by the fit of F_{pl} values to the following model,

$$F_{pl} = c_1\,|\cos(\theta)^2| + c_2\,|\cos(\theta)^2|, \tag{3.3}$$

where θ is the polarization angle of the incident field and the asymmetric terms, $c_2\,c_1$, are due to beam displacement by rotation of the half-wave plate. The slight discrepancy between $\theta = 0°$ and $\theta = 180°$ can be traced to a $\sim 1\mu$m displacement of the focused incident light on the grating as the half-wave plate is rotated, due to deviation of the transmitted beam by 1 arc minute (within the manufacturers specification) before focusing with the high NA objective. As in the radiation, the field emission is determined by the launching of SPPs. However, the focusing of SPPs on the emitting singularity(ies) and the exponential dependence of field-emission on local field (Eq. **??**), appears to makes it sensitive to the path the SPP takes on the rough surface.

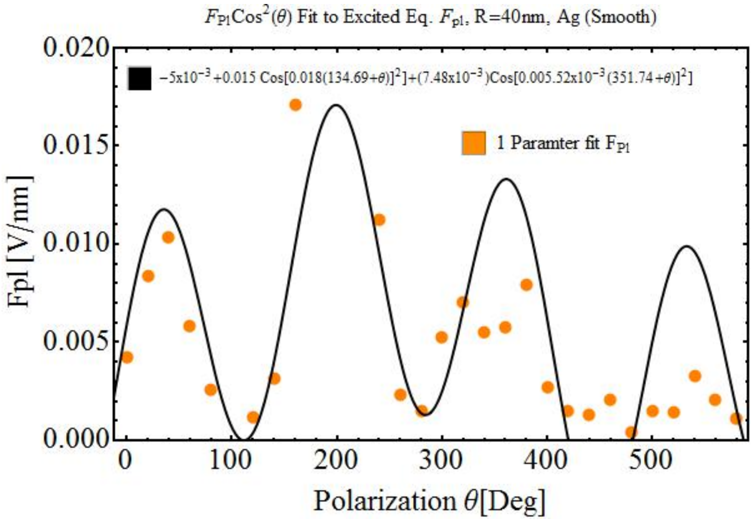

Figure 3.15: F_{pl} values from the Excited model, Eq. (3.1a),vs. polarization angle and fit to Eq.(3.2.1)

The results from this tip show a clear proof of principle and hint at favoring one of the two physical descriptions discussed, but a larger dynamic range of data and more confidence in structural (geometric) variables would be needed discern a mechanism from measurements. In an effort to increase superfocusing efficiency and measure in regimes where current is stable in time, deliver higher plasmon fields to the apex, and therefore allow for a larger range of current to be measured before the static FE threshold, I developed the FIB lathe method outlined at the beginning of this chapter so that the probe tips under investigation could be reliably produced with defect-free surfaces over the entire length between the grating and the apex.

3.2.2 Nano-lathed Tips

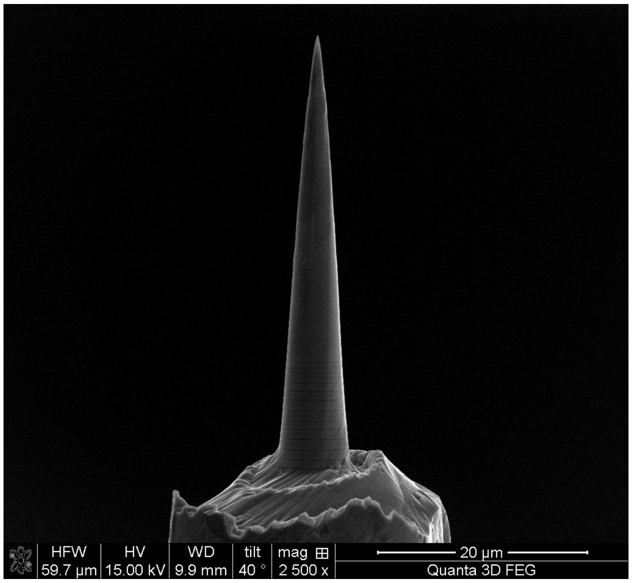

Figure 3.16: First lathed silver tip, with apex of radius $\sim 20\,\text{nm}$.

The first defect-free tip made with the lathe technique had an apex radius $\sim 20\,\text{nm}$.The parallel, 50 nm deep grating was placed 40 µm from the apex. After coupling was found and maximized with light measurements, the grating was illuminated with 7 mW ($\sim$0.35 $\text{V}\,\text{nm}^{-1}$)).

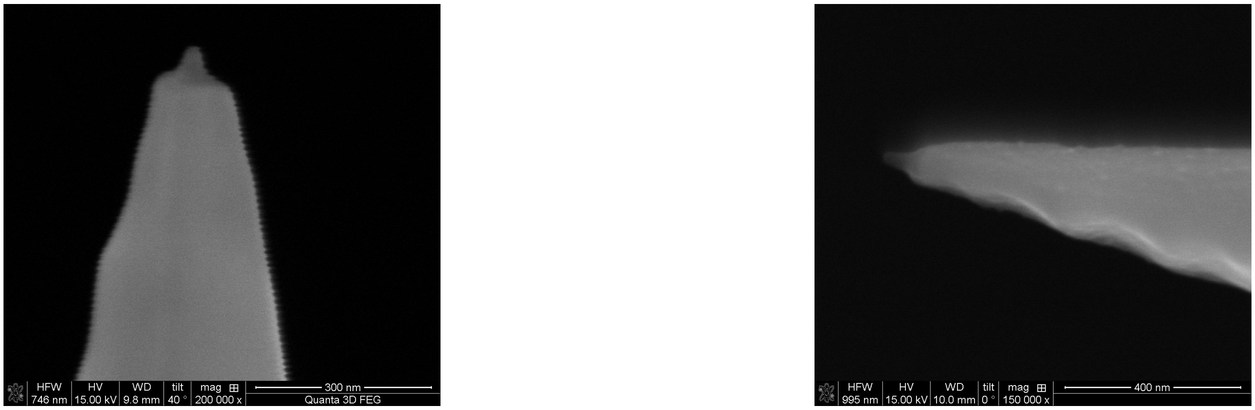

(a) SEM image of apex before current measurements.

(b) SEM image of apex after measurements.

Figure 3.17: Lathed Silver Tip Apex - before and after measurements

Some measurements recorded smaller current at low voltage ($\sim$100 V), transient in time relative to full acquisitions times, in additional to the familiar exponentially dependent current at higher (450-600 V) bias. For incident power in the range of 7 mW, low-bias current observed was mostly transient attributed to transient structures local to the incident field as this current was also more sensitive to small fluctuations (∼200 nm) in incident laser position than was the light. SEM images taken after these initial observations verified the grating remained damage free, but did show the formation of small (<∼10 nm) features around the apex, while maintaining overall structural integrity. This is currently thought to be related to gallium implantation resulting from the ion etching process, but will addressed in subsequent investigations.

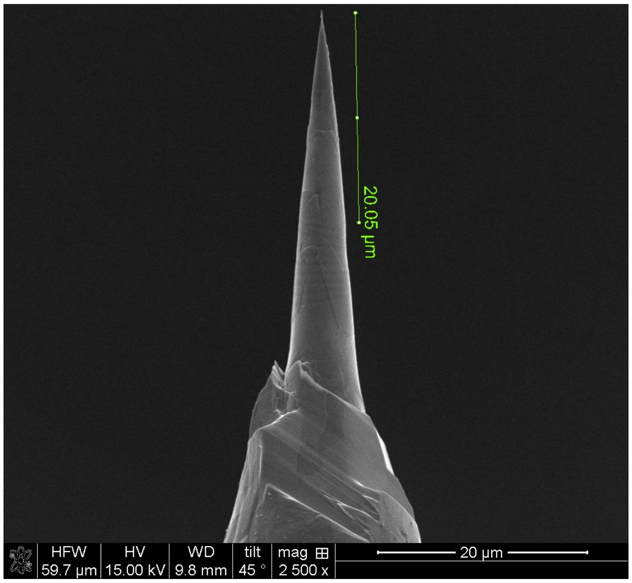

Figure 3.18: FIB lathed gold tip with apex of radius ∼ 15 nm and fan shaped grating separated by 20 µm.

To compare to the the silver, a gold tip was made by the same method, shown in Fig. lathegoldSEM1. The propagation length (see Eq. (1.5b)) of gold is shorter than silver for the same ω_{spp}, but gold's inert and more robust characteristics gave it the potential to provide improved waveguiding for the SPP. Gratings on the gold tips were etched 20 µm from the apex. Otherwise, the experimental methods for gold tips were identical to those for silver. FIB lathed gold tip,shown in Fig.(3.18), with apex of radius ∼ 15nm and fan shaped grating separated by 20 µm. The grating here was illuminated with 5 mW average power.

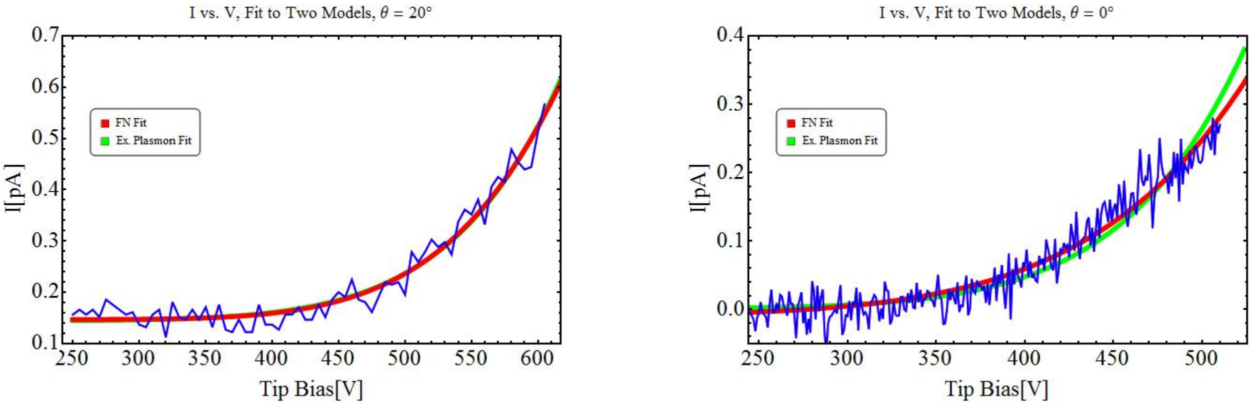

(a) Raw data (blue) and fits to both models for smooth Ag tip, at $\theta = 20°$.

(b) Raw data (blue) and fits to both models for smooth Au tip $\theta = 0°$.

Figure 3.19: Example of raw data and fits on Ag tip, for $\theta = 20°$, and a smooth Au tip, $\theta = 0°$

The results show the same polarization dependence to that of the rough etched tip. The extracted values for Ag of a vs. polarization angle are shown for three values of β fit to the Fermi and the excited tunneling equations, Fig. 3.20.

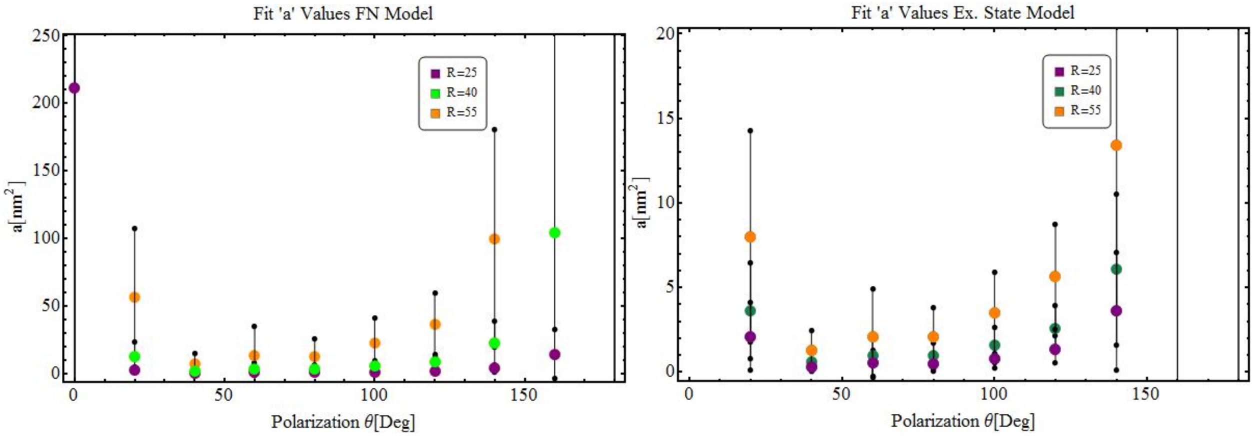

(a) Resulting values of a values vs. polarization angle from fits to the Fermi model, Eq. (3.1a), for 3 values of $\beta = kR$ for $R = 30\,\text{nm}, 40\,\text{nm}$, and $50\,\text{nm}$.

(b) Resulting values of a vs. polarization angle from fits to the Excited level model, Eq. (3.1b) for 3 values of $\beta = kR$ forfor $R = 30\,\text{nm}, 40\,\text{nm}$, and $50\,\text{nm}$.

Figure 3.20: a values vs. polarization angle from fits to both models for current.

Average A, Ag Tip (Machined)		
R(nm)	A_{FN}(nm^2)	$A_{j(1.5eV)}$(nm^2)
30	4.67×10^3	2.97×10^3
40	5.30×10^5	2.19×10^5
50	3.59×10^6	5.09×10^5

Table 3.2: A values used in 1-parameter fits. These values are average values for the median 30 percent of a values, to include only those values with the most statistically meaningful fitting results, converted to actual emitting area.

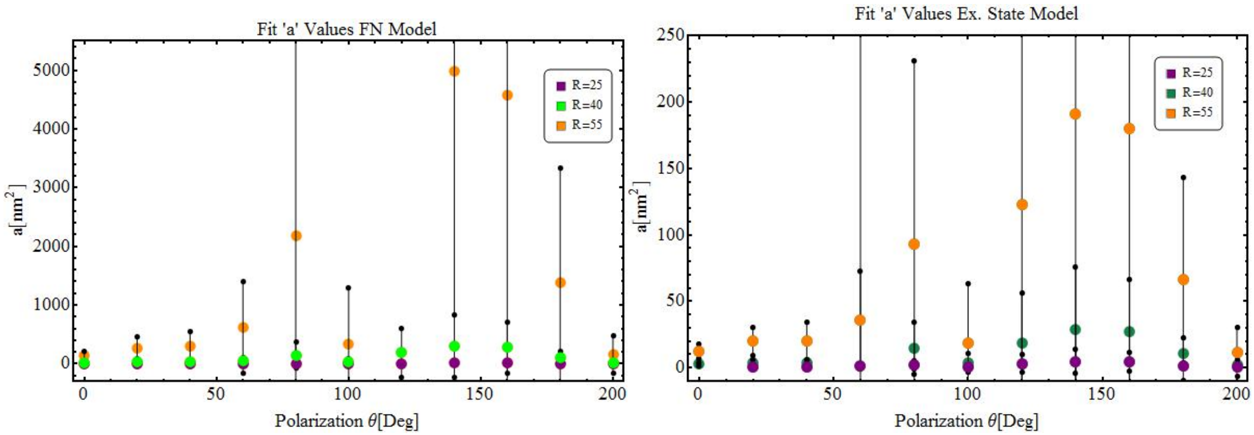

(a) Resulting values of a values vs. polarization angle from fits to the Fermi model, Eq. (3.1a), for 3 values of $\beta = kR$ for $R = 25\,\text{nm}(a_{av} = 5.33 \times 10^3)$, $40\,\text{nm}(a_{av} = 1.14 \times 10^5)$, and $55\,\text{nm}(a_{av} = 1.40 \times 10^6)$.

(b) Resulting values of a vs. polarization angle from fits to the Excited level model, Eq. (3.1b) for 3 values of $\beta = kR$ for $R = 25\,\text{nm}\,(a_{av} = 2.04 \times 10^4)$, $40\,\text{nm}\,(a_{av} = 1.82 \times 10^5)$, and $55\,\text{nm}\,(a_{av} = 1.05 \times 10^5)$.

Figure 3.21: a values vs. polarization angle from fits to both models for current.

We see in Fig.(3.20) that statistical errors are still large relative to the values, but much smaller overall, along with the values themselves, similarly for gold, shown in Fig.3.21b. The emitting area values for each tip are given in Tables 3.2 and 3.3.

For the single parameter fits, more reliable trends in comparing the two models are apparent. Fig. 3.22 shows the one parameter fitting values for F_{Pl} for both models, for the median fit R (and therefore β) value, $R = 40\,\text{nm}$, now with two orders of magnitude difference of

Average A, Au Tip (Machined)		
R(nm)	A_{FN}(nm^2)	$A_{j(1.5eV)}$(nm^2)
25	237.9	24.9
40	1.75×10^3	759.8
55	1.02×10^3	1.03×10^4

Table 3.3: A values used in 1-parameter fits. These values are average values for the top 70 percent of a values, to include only those values with the most statistically meaningful fitting results, converted to actual emitting area.

values. For this tip, values of emitting area are in physically appropriate regimes for the smooth and more even structure.

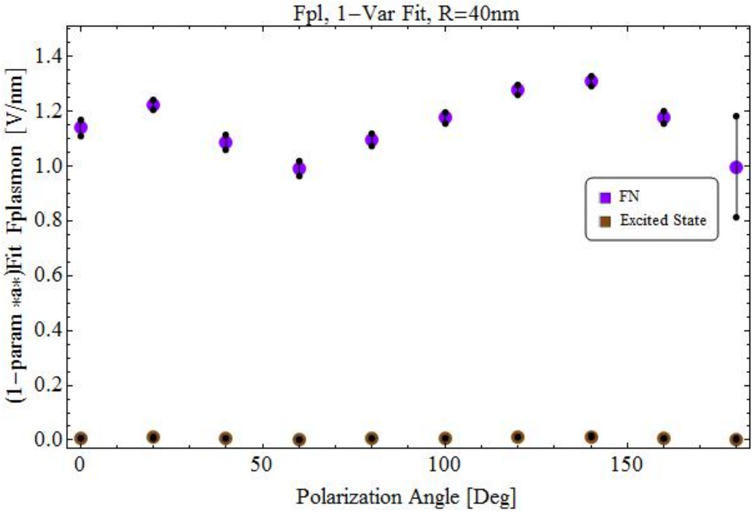

Figure 3.22: F_{pl} values vs. polarization angle given by both models using radius, $R = 40\,\text{nm}$.

The local plasmon field, F_{pl}, varies with a similar $\cos^2(\theta)$ dependence, shown Fig. 3.23 for the silver tip, fit now to a simpler model for the half-rotation of the half waveplate these measurements span, given by:

$$F_{pl} = c_1 \, |\cos(\theta)^2|. \tag{3.4}$$

Signal to noise for these data was increased by a factor of ~ 2, however we found the silver tips etched by the lathe process often to be unstable, however more so in showing large morphology changes with measurements than complete destruction by arcing. Gallium implantation into the silver during the lathe process could account for this behavior and is currently under investigation. Because of the different structure and eutectic properties of gold, tips were subsequently made using the lathe process from gold and measured in the same manner.

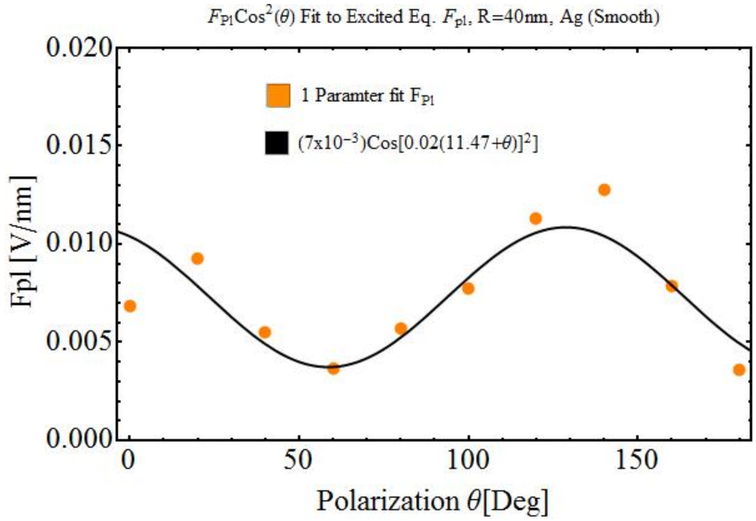

Figure 3.23: F_{Pl} values vs. polarization angle from fits to both models for current.

Finally, we can again plot the contributions for each model, Fig. 3.24 and see for these tips the insignificant Fermi contributions to the excited model and the range of voltage that would have been necessary to see the trends diverge.

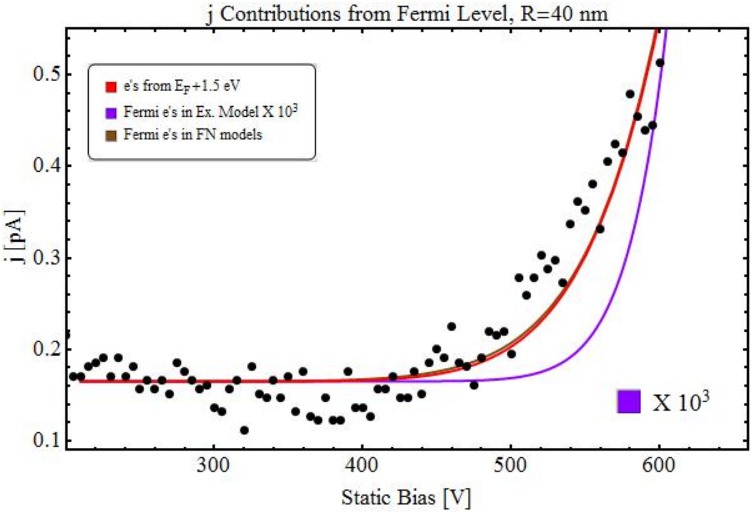

Figure 3.24: Calculated current from Fermi tunneling in the excitation model and that from each model alone for relevant range of applied DC voltage. $R = 40\,\mathrm{nm}$, $A_{j(1.5eV)} = 2.19 \times 10^5\,\mathrm{nm}^2$

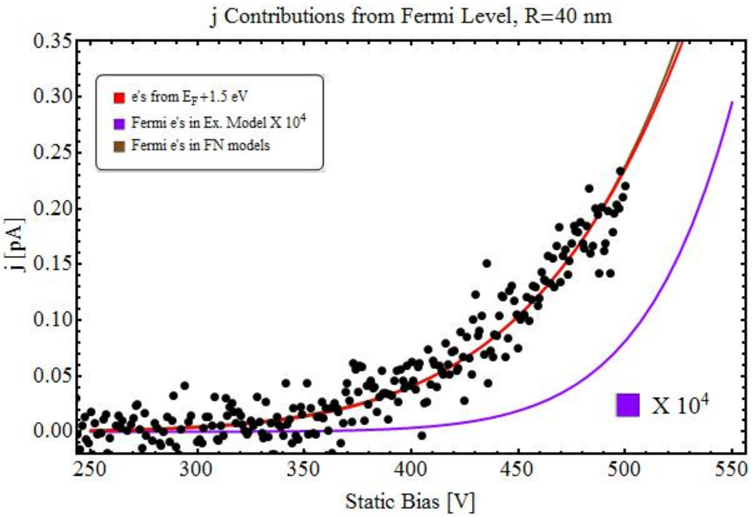

Figure 3.25: Calculated current from Fermi tunneling in the excitation model and that from each model alone for relevant range of applied DC voltage. $R = 40\,\text{nm}$

From which the average A values, now from the top 70% of fit values, found in Table 3.3.

We can also see directly the relative effect the initial value of R (or β) has on the two models. Comparing results for two radii, Fig.3.26, it follow the larger R (smaller β) produces smaller a smaller field for a given bias and plays a smaller role relative to the plasmon filed.

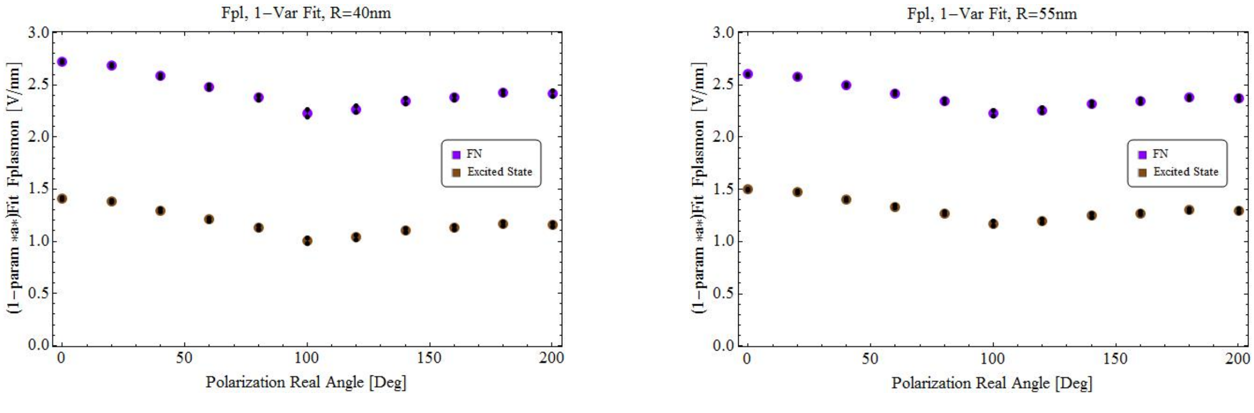

(a) F_{pl} values vs. polarization angle given by both models using radius, $R = 40\,\text{nm}$ for a gold tip.

(b) F_{pl} values vs. polarization angle given by both models using radius, $R = 55\,\text{nm}$ for a gold tip.

Figure 3.26: Change in model comparison values for 2 values of R.

3.3 Final Remarks

Investigation of nonlocal charge excitations on STM probe tips has established proof of principle that electrons are field emitted upon superfocusing of SPPs at the tip apex,. Using gold and silver tips fabricated either by electrochemical etching or FIB nano machining, we have observed field emission driven by SPPs launched via grating coupling of 20 fs Ti:Sapph laser pulses, 20 to 30 µm removed from the apex. Although an extractor field was required to assist the plasmon driven field emission, the process could be verified by concurrent measurements of current and radiation of light from the apex.

Ultimately, the field emission current is determined by the net field reached at the apex, as a result of the competition from the geometrical focusing of the cone and scattering and radiative losses during propagation. The large fields required for emission (5 V/nm), make this nonlinear tunneling process sensitive to asperities on the surface. On electrochemically etched silver tips, where asperities ranging from atomic scale to 100 nm scale decorate the surface, large extraction fields of order $\sim 2 - 4\,\mathrm{V\,nm^{-1}}$ were needed to generate observable current (0.1- 1 pA). Despite the limited dynamic range of the data, the I/V curves obtained as a function of polarization angle and laser intensity, could be analyzed to conclude that the tip acts as a large area emitter. This is consistent with the observation of light radiated from µm-scale area of the tip cone..

After developing a method to micro-machine probe tips using FIB methods, the experiment was repeated using relatively defect free cones of silver and gold. Despite the smooth surface, large extractor fields remained necessary to obtain measurable current. The larger dynamic range of this data, and the extracted emission areas in agreement with the SEM images, afforded greater certainty in the assignment of the process to tunneling emission localized to the tip apex.

The results from this investigation highlight the need for further investigation. We do not understand the losses associated with the propagation of the SPPs, which appear to be significantly larger than theoretical expectations. We suspect Ga implantation during the FIB processing to be a major culprit. Also, we do not yet understand the need for large extractor fields when directly irradiating the apex. Field ionization in the limited vacuum of the cell (10×10^{-5}Torr) could explain the inefficiency of collection. We have since reduced the base pressure by 3 orders of magnitude. Given the measurements in the absence of an extractor much larger dynamic range can be expected in the measurements; moreover, unique models can be assigned to field emission with remotely launched plasmons. Finally, simultaneous recording of laser induced and DC-driven field emission could provide an internal reference to extract model parameters with greater certainty. These improvements in measurement will be made, and a more complete model of the entire process will be constructed in future work.

Bibliography

[1] *Field Emission.* 1980.

[2] B Barwick, C Corder, J Strohaber, N Chandler-Smith, C Uiterwaal, and H Batelaan. Laser-induced ultrafast electron emission from a field emission tip. *New Journal of Physics*, 9(5):142–142, May 2007.

[3] Samuel Berweger, Joanna M. Atkin, Robert L. Olmon, and Markus B. Raschke. Light on the Tip of a Needle: Plasmonic Nanofocusing for Spectroscopy on the Nanoscale. *The Journal of Physical Chemistry Letters*, 3(7):945–952, April 2012.

[4] G. Binnig, H. Rohrer, Ch. Gerber, and E. Weibel. Surface studies by scanning tunneling microscopy. *Phys. Rev. Lett.*, 49:57–61, Jul 1982.

[5] G. Binnig, H. Rohrer, Ch. Gerber, and E. Weibel. Tunneling through a controllable vacuum gap. *Applied Physics Letters*, 40(2), 1982.

[6] Péter Dombi, Anton Hörl, Péter Rácz, István Márton, Andreas Trügler, Joachim R Krenn, and Ulrich Hohenester. Ultrafast strong-field photoemission from plasmonic nanoparticles. *Nano letters*, 13(2):674–8, February 2013.

[7] D.M. Eigler and E.K. Schweizer. Positioning single atoms with a scanning tunnelling microscope. *Nature*, 344:524–526, 1990.

[8] R. H. Fowler and L. Nordheim. Electron Emission in Intense Electric Fields. *Proceedings of the Royal Society A: Mathematical, Physical and Engineering Sciences*, 119(781):173–181, May 1928.

[9] L. R. Harriott and M. J. Vasile. Focused ion beam secondary ion mass spectrometry: Ion images and endpoint detection. *Journal of Vacuum Science and Technology B*, 7(2), 1989.

[10] G. Herink, D. R. Solli, L. Wimmer, M. Gulde, K. Echternkamp, S. V. Yalunin, R. Bormann, and C. Ropers. Photoemission at metallic nanostructures: multiphoton and strong-field dynamics. 8623:862311, March 2013.

[11] Peter Hommelhoff, Yvan Sortais, Anoush Aghajani-Talesh, and Mark A. Kasevich. Field Emission Tip as a Nanometer Source of Free Electron Femtosecond Pulses. *Physical Review Letters*, 96(7):1–4, February 2006.

[12] Peter Hommelhoff, Yvan Sortais, Anoush Aghajani-Talesh, and Mark A. Kasevich. Field emission tip as a nanometer source of free electron femtosecond pulses. *Phys. Rev. Lett.*, 96:077401, Feb 2006.

[13] P.B. Jhonson and R.W. Christy. Optical constants of the noble metals. *Phys. Rev. B*, 6(12):4370–4379, October 1972.

[14] Hiroyuki Kawano. Effective work functions for ionic and electronic emissions from mono- and polycrystalline surfaces. *Progress in Surface Science*, 83(1-2):1–165, February 2008.

[15] L. Keldysh. *Sov. Phys. JETP*, page 1307.

[16] H. Kroemer and R. E. Burgess. Corrected Values of Fowler-Nordheim. *Physical Review*, 90(4):515, 1953.

[17] M Krüger, M Schenk, M Förster, and P Hommelhoff. Attosecond physics in photoemission from a metal nanotip. *Journal of Physics B: Atomic, Molecular and Optical Physics*, 45(7):074006, April 2012.

[18] Fumiya Kusa, Katharina Echternkamp, Georg Herink, Claus Ropers, and Satoshi Ashihara. Photoelectron emission from resonant nanoantennas driven by femtosecond mid-infrared pulses. In *19th International Conference on Ultrafast Phenomena*, page 08.Tue.B.4. Optical Society of America, 2014.

[19] Stephan Link and Mostafa A El-sayed. Spectral Properties and Relaxation Dynamics of Surface Plasmon Electronic Oscillations in. *J. Phys. Chem. B*, 103:8410–8426, 1999.

[20] Michael K Miller, Kaye F Russell, Keith Thompson, Roger Alvis, and David J Larson. M icroscopy M icroanalysis Review of Atom Probe FIB-Based Specimen Preparation Methods. pages 428–436, 2007.

[21] H. Raether. *Surface Plasmons.* Springer-Verlag, Berlin, 1988.

[22] Bin Ren, Gennaro Picardi, and Bruno Pettinger. Preparation of gold tips suitable for tip-enhanced Raman spectroscopy and light emission by electrochemical etching. *Review of Scientific Instruments*, 75(4):837, 2004.

[23] C. Ropers, C. C. Neacsu, T. Elsaesser, M. Albrecht, M. B. Raschke, and C. Lienau. Grating-coupling of surface plasmons onto metallic tips: a nanoconfined light source. *Nano letters*, 7(9):2784–8, September 2007.

[24] C. Ropers, D. R. Solli, C. P. Schulz, C. Lienau, and T. Elsaesser. Localized Multiphoton Emission of Femtosecond Electron Pulses from Metal Nanotips. *Physical Review Letters*, 98(4):1–4, January 2007.

[25] Claus Ropers, Thomas Elsaesser, Giulio Cerullo, Margherita Zavelani-Rossi, and Christoph Lienau. Ultrafast optical excitations of metallic nanostructures: from light confinement to a novel electron source. *New Journal of Physics*, 9(10):397–397, October 2007.

[26] Markus Schenk, Michael Krüger, and Peter Hommelhoff. Strong-Field Above-Threshold Photoemission from Sharp Metal Tips. *Physical Review Letters*, 105(25):1–4, December 2010.

[27] C Sonnichsen, T Franzl, T Wilk, G von Plessen, and J Feldmann. Plasmon resonances in large noble-metal. *New Journal of Physics*, 4(93):1–8, 2002.

[28] Mark Stockman. Nanofocusing of Optical Energy in Tapered Plasmonic Waveguides. *Physical Review Letters*, 93(13):1–4, September 2004.

[29] M. J. Vasile, D. a. Grigg, J. E. Griffith, E. a. Fitzgerald, and P. E. Russell. Scanning probe tips formed by focused ion beams. *Review of Scientific Instruments*, 62(9):2167, 1991.

[30] Hirofumi Yanagisawa, Christian Hafner, Patrick Don, Martin Kl, Thomas Greber, and Matthias Hengsberger. Laser-induced Field Emission from Tungsten Tip: Optical Control of Emission Sites and Emission Process. *Physical Review B*, 81:1–12, 2010.

[31] Hirofumi Yanagisawa, Matthias Hengsberger, Dominik Leuenberger, Martin Klöckner, Christian Hafner, Thomas Greber, and Jürg Osterwalder. Energy Distribution Curves of Ultrafast Laser-Induced Field Emission and Their Implications for Electron Dynamics. *Physical Review Letters*, 107(8):1–5, August 2011.

[32] Anatoly V. Zayats, Igor I. Smolyaninov, and Alexei a. Maradudin. Nano-optics of surface plasmon polaritons. *Physics Reports*, 408(3-4):131–314, March 2005.

[33] C Zhang, B Gao, L G Chen, Q S Meng, H Yang, R Zhang, X Tao, H Y Gao, Y Liao, and Z C Dong. Fabrication of silver tips for scanning tunneling microscope induced luminescence. *The Review of scientific instruments*, 82(8):083101, August 2011.

[34] Jorge Zuloaga, Emil Prodan, and Peter Nordlander. Quantum plasmonics: optical properties and tunability of metallic nanorods. *ACS nano*, 4(9):5269–76, September 2010.